



Energy transfer mechanisms in adverse pressure gradient turbulent boundary layers: production and inter-component redistribution

Taygun R. Gungor^{1,2}, Yvan Maciel² and Ayse G. Gungor^{1,†}

¹Faculty of Aeronautics and Astronautics, Istanbul Technical University, 34469 Maslak, Istanbul, Turkey

²Department of Mechanical Engineering, Laval University, Quebec City, QC, Canada G1V 0A6

(Received 3 December 2021; revised 30 May 2022; accepted 22 July 2022)

Production and inter-component redistribution of turbulence in adverse pressure gradient (APG) turbulent boundary layers (TBLs) with small and large velocity defects are investigated, along with the structures playing a role in these energy transfer mechanisms. We examine the wall-normal and spectral distributions of energy, production and pressure-strain in APG TBLs, and compare these distributions with those in canonical flows. It is found that the spectral distributions of production and pressure-strain are not affected profoundly by an increase of the velocity defect, although the energy spectra change drastically in the inner layer of the large-defect APG TBL. In the latter, the signature of the inner-layer streaks is absent from the energy spectra. In the outer layer, energetic, production and pressure-strain structures appear to change from wall-attached to wall-detached structures with increasing velocity defect. Despite this, the two-dimensional spectral distributions have similar shapes and wavelength aspect ratios of the peaks in all these flows. Therefore, the conclusion is that the mechanisms responsible for turbulence production and inter-component energy transfer may remain the same within each layer in all these flows. It is the intensity of these mechanisms within one layer that changes with velocity defect, because of the local mean shear variation.

Key words: turbulent boundary layers

1. Introduction

When a turbulent boundary layer (TBL) is subjected to a sufficiently strong or prolonged adverse pressure gradient (APG), its mean momentum defect increases. This growing

† Email address for correspondence: ayse.gungor@itu.edu.tr

defect changes the nature of the flow progressively, hence APG TBLs become different from canonical wall-bounded flows such as zero pressure gradient (ZPG) TBLs or channel flows.

Indeed, the change in the mean velocity profile leads to a different distribution of the mean shear in the wall-normal direction, which in turn affects the turbulent energy distribution in the boundary layer. With less mean shear, the turbulent activity in the inner layer decreases (Skåre & Krogstad 1994; Elsberry *et al.* 2000), and the inner maximum of Reynolds stresses vanishes in the case of large velocity defect TBLs (Maciel, Rossignol & Lemay 2006b; Gungor *et al.* 2016; Maciel *et al.* 2018). The outer-layer turbulence, on the other hand, becomes dominant when the velocity defect is important, and a turbulence production peak emerges in the outer layer (Skåre & Krogstad 1994; Gungor *et al.* 2016).

In the inner layer, the impact of the pressure gradient on the coherent structures also depends on the extent of the mean velocity defect. The spanwise and streamwise sizes of the most energetic $\langle u^2 \rangle$ -carrying structures do not change significantly when the defect is small (Harun *et al.* 2013; Lee 2017). As in canonical flows, the inner peak of the energy spectra of $\langle u^2 \rangle$ is at inner-scaled spanwise wavelength (λ_z^+) approximately 120 (Lee 2017; Tanarro, Vinuesa & Schlatter 2020) and inner-scaled streamwise wavelength (λ_x^+) approximately 1000 (Harun *et al.* 2013; Sanmiguel Vila *et al.* 2020a). Furthermore, the shape of the $\langle u^2 \rangle$ spectra is similar in ZPG and small-defect APG TBLs (Harun *et al.* 2013; Tanarro *et al.* 2020). When the defect is large, spatial organization and spectral features of the energetic structures change in the inner layer. The near-wall streaks are weakened (Skote & Henningson 2002; Lee & Sung 2009). They also become more irregular, disorganized and less streaky (Lee & Sung 2009; Maciel, Gungor & Simens 2017a), and even vanish at separation (Rahgozar & Maciel 2012). Moreover, the inner peak in the $\langle u^2 \rangle$ spectra, which is connected to the streaks, vanishes in the large-defect case (Kitsios *et al.* 2017; Lee 2017). Apart from the changes in the streaks, Maciel *et al.* (2017a) and Maciel, Simens & Gungor (2017b) reported that sweeps and ejections are weaker in the inner layer than in the outer layer in large-defect TBLs, and their number is fewer than in ZPG TBLs.

The elevated outer-layer turbulence activity in APG TBLs was reported numerous times regardless of the velocity defect (Harun *et al.* 2013; Lee 2017; Tanarro *et al.* 2020). The $\langle u^2 \rangle$ spectra show that the energetic outer layer structures are longer and wider than their counterparts in the inner layer in APG TBLs (Harun *et al.* 2013; Kitsios *et al.* 2017). The outer peak of the spectra is at $\lambda_x/\delta \approx 3$ (Harun *et al.* 2013; Sanmiguel Vila *et al.* 2020a) and $\lambda_z/\delta \approx 1$ (Bobke *et al.* 2017; Lee 2017), where δ is the boundary layer thickness. Elevated outer-layer activity is also reported for high-Reynolds-number canonical flows (Hutchins & Marusic 2007b; Marusic, Mathis & Hutchins 2010a) with an outer peak in the $\langle u^2 \rangle$ spectra due to elongated, meandering structures (Marusic *et al.* 2010a), which are called superstructures in external flows (Hutchins & Marusic 2007a) and very-large-scale motions (VLSMs) in internal flows (Kim & Adrian 1999). The streamwise wavelength of the outer peak in the energy spectra of $\langle u^2 \rangle$, which is associated with these structures, is of the order of 6δ in boundary layers (Smits, McKeon & Marusic 2011). There is also another type of structure, called large-scale motions (LSMs), associated with smaller wavelengths $\lambda_x/\delta \approx 2-3$ (Smits *et al.* 2011). The energetic outer-layer structures in APG TBLs are more similar to LSMs than superstructures/VLSMs in terms of dimensions. However, Sanmiguel Vila *et al.* (2020a) investigated the effects of APG and high Reynolds number for small-defect APG TBLs and found two outer peaks (one similar to that of ZPG superstructures, and the typical APG one) in the $\langle u^2 \rangle$ spectra at sufficiently high Reynolds number. Regarding the magnitude of the typical APG outer

peak, several studies have reported its increase with increasing velocity defect (Lee 2017; Sanmiguel Vila *et al.* 2020b) when the levels are normalized with friction-viscous scales. However, such a conclusion could be an artefact of using the friction-viscous scales because they are not proper scales for energy levels for APG TBLs (Gungor *et al.* 2016), especially for large-defect ones (Maciel *et al.* 2018).

The turbulence regeneration mechanisms, or in other words, self-sustaining mechanisms, have been studied extensively in canonical flows. However, studies concerning APG TBLs are rather scarce. One of the mechanisms that has been suggested for APG TBLs is the instability of streaks (Marquillie, Ehrenstein & Laval 2011), which was already considered as a regeneration mechanism for canonical wall-bounded flows (Hall & Horseman 1991). Another mechanism proposed for the outer region of large-defect APG TBLs is an inflectional instability associated with the outermost inflection point of the mean velocity profile, which is inviscidly unstable. Elsberry *et al.* (2000) suggested that such an instability affects the flow field in their large-defect APG TBL. The location of the inflection point was close to that of the maxima of the Reynolds normal stresses and turbulent kinetic energy production. The presence of an inflection point at the same wall-normal location as the peak of the Reynolds stresses was reported by other researchers as well (Gungor *et al.* 2016; Kitsios *et al.* 2017). Furthermore, Schatzman & Thomas (2017) suggested that an embedded shear layer, which is centred around the aforementioned inflection point in the outer layer, exists in APG TBLs. They proposed scaling parameters based on this idea of an embedded shear layer and obtained self-similar mean velocity and Reynolds stress profiles in their large-defect APG TBL, as well as in other large-defect cases. Balantrapu *et al.* (2021) also obtained self-similar profiles with the same scaling in their highly decelerated axisymmetric turbulent boundary layer. However, Maciel *et al.* (2017a) noted that they could not find any roller-like structures that are the sign of a Kelvin–Helmholtz type instability. In addition, it is important to note that moderate-defect APG TBLs have an outer maximum of the Reynolds stresses without the presence of an inviscidly unstable inflection point in the mean velocity profile (Maciel *et al.* 2018). It is still not known whether an inflection point instability exists, and furthermore if it is directly responsible for turbulent regeneration in large-defect APG TBLs, but it is possible that the presence of Reynolds stress peaks and an inflection point in the outer layer is simply correlated without any causality (Balantrapu *et al.* 2021).

From a different perspective that does not necessarily involve an inflectional instability, several researchers have reported that APG TBLs with large velocity defect might behave like free shear flows due to the change in the mean velocity (Gungor *et al.* 2016; Kitsios *et al.* 2017). Gungor, Maciel & Gungor (2020) demonstrated that the Reynolds shear stress carrying structures in large-defect APG TBLs and homogeneous shear turbulence flow, which has no inflection point, have similar shapes and are mostly dependent on the local mean shear. These studies suggest that self-sustaining mechanisms might be similar in the outer layer of large-defect APG TBLs and free shear flows, and highlight the causal role played by mean shear.

The task of identifying the self-sustaining mechanisms present in APG TBLs is a formidable one. A first step along that route is to better understand the energy transfers resulting directly from the self-sustaining processes, namely turbulence production and energy transfer between Reynolds stress components (the pressure-strain term in the Reynolds stress transport equations). Examining the wall-normal distributions of production and pressure-strain does not suffice for that purpose. A more complete picture can be obtained by also investigating the spectral distributions, among scales and position, of these energy transfers. The idea of studying the spectra of the terms in the Reynolds stress transport equations was introduced first by Lumley (1964), and it has

gained attention recently. The spectra of the turbulent kinetic energy or Reynolds stress transport equations have been utilized to examine spatial transport, energy cascade or scale separation in channel flows (Mizuno 2016; Cho, Hwang & Choi 2018; Lee & Moser 2019), Couette flows (Kawata & Alfredsson 2018), ZPG TBLs (Chan, Schlatter & Chin 2021) or separating and reattaching flows (Gatti *et al.* 2020). As mentioned above, in the present work we focus on the spectral features of production and pressure-strain with the aim of better understanding the self-sustaining mechanisms present in APG TBLs.

More precisely, the goal of this study is to examine the spectral distributions of energy, production and pressure-strain in inner and outer layers of APG TBLs, and compare them with the ones in canonical wall-bounded flows to better understand the mechanisms involved. We consider both small and large velocity defect cases to analyse the effect of velocity defect on these energy transfer mechanisms.

2. Databases

We utilized three types of flows in this paper: APG TBLs, ZPG TBLs and channel flows. A new direct numerical simulations (DNS) database is generated for APG TBLs. This new database is an extension of the database that was introduced by Gungor *et al.* (2017) and analysed by Maciel *et al.* (2018), which was referred to as DNS2017. The main difference between the new database and DNS2017 is that the new database has a wider spanwise width and a slightly different pressure gradient distribution. Both flow cases are nonetheless almost identical in terms of mean velocity and Reynolds stress distributions, and two-point correlations. Since they are almost identical, here we will use only the most recent one. The details of the databases employed in this paper are given in the following subsections.

2.1. The current APG TBL database

The current database is a DNS database of a non-equilibrium APG TBL with a Reynolds number based on momentum thickness (Re_θ) reaching up to 8000. The code used to perform the DNS solves the three-dimensional incompressible Navier–Stokes equations. It provides the time evolution of three-dimensional velocity and pressure fields for a given flow configuration. The DNS code employs a hybrid MPI/OpenMP approach for parallelization. Further details on the code can be found in Simens *et al.* (2009) and Borrell, Sillero & Jiménez (2013).

The DNS computational set-up consists of two simulation domains, the auxiliary and main domains, running concurrently as described in Sillero, Jiménez & Moser (2013) and Gungor *et al.* (2016). The auxiliary ZPG TBL DNS, with a coarser resolution, are intended to provide the realistic turbulent inflow data for the main APG TBL DNS. The goal of using two domains is to provide inflow conditions for the main DNS with lower computational cost. Regarding the other boundary conditions, the bottom surface is a flat plate with a no-slip boundary condition. The side boundary conditions are periodic. The far-field boundary condition is adjusted in the form of suction and blowing to apply adverse/favourable pressure gradients. The outflow condition is a Neumann boundary condition. The computational domain of the main APG TBL simulation, a rectangular volume with streamwise, wall-normal and spanwise lengths $(L_x, L_y, L_z)/\delta_{av} = (25.3, 4.8, 7.1)$, is discretized with $N_x \times N_y \times N_z = 4609 \times 736 \times 1920$ grid points. Here, the average boundary layer thickness (δ_{av}) is calculated within the useful range (or so-called domain of interest), which is the zone between the vertical dashed lines in figure 1.

Production and inter-component redistribution of turbulence in APG TBL

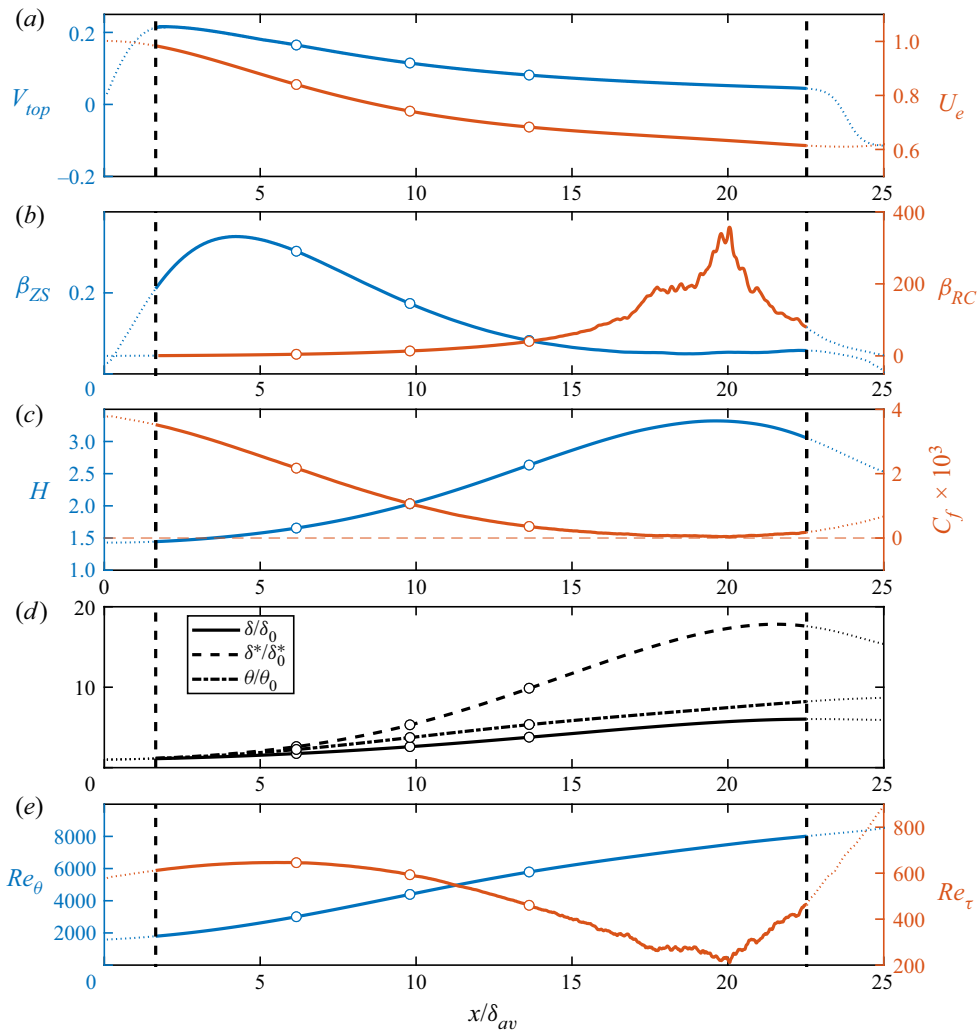


Figure 1. Streamwise development of the main parameters of the APG TBL. (a) The suction/blowing boundary condition V_{top} and edge velocity U_e . (b) Pressure gradient parameters β_{ZS} and β_{RC} . (c) Shape factor H and skin friction coefficient C_f . (d) Parameters δ , δ^* and θ normalized with their values at inlet. (e) Reynolds numbers Re_θ and Re_τ . The vertical dashed lines are the boundaries of useful range. The open circles denote the three streamwise positions that are used in the paper.

Figure 1 shows the spatial development of main parameters of the APG TBL. As stated before, the pressure gradient in the APG TBL is generated by imposing a suction/blowing boundary condition for the wall-normal component of the velocity at the top boundary (V_{top}). Figure 1(a) shows the spatial development of V_{top} along with the edge velocity U_e . The definition of U_e is not straightforward in flows with inviscid velocity that varies in the wall-normal direction, such as the current flow. Although it is not the most generally applicable definition (see, for instance, Griffin, Fu & Moin 2021), we utilize the maximum streamwise component of the mean velocity in the wall-normal direction as U_e for this study, to be consistent with most of the literature (Gungor *et al.* 2016; Maciel *et al.* 2018) and because it works for the flow cases studied here.

At the beginning of the domain, the suction velocity increases sharply within a short distance to impose the desired pressure gradient distribution. Downstream of this region, the suction velocity is adjusted to obtain a regularly increasing shape factor H (figure 1c). The change in V_{top} near the end of the computational domain is to increase the numerical stability of the simulation by accelerating the flow so that the Neumann boundary condition still holds. The suction boundary condition decelerates the flow, which is seen from the development of the edge velocity U_e in figure 1(a).

Figure 1(b) shows two pressure gradient parameters that characterize the effect of the pressure gradient on the outer layer: β_{RC} , the Rotta–Clauser pressure gradient parameter, and β_{ZS} , the pressure gradient parameter based on the Zagarola–Smits velocity, defined as

$$\beta_{RC} = \frac{\delta^*}{\rho u_\tau^2} \frac{dP_e}{dx}, \quad \beta_{ZS} = \frac{\delta}{\rho U_{ZS}^2} \frac{dP_e}{dx}. \quad (2.1a,b)$$

Here, δ^* is the displacement thickness, ρ is the density, u_τ is the friction velocity, P_e is the pressure at the edge of the boundary layer, and U_{ZS} is the Zagarola–Smits velocity ($U_{ZS} = U_e \delta^* / \delta$) (Zagarola & Smits 1998). The traditionally used pressure gradient parameter, β_{RC} , increases progressively until β_{RC} is above 350, and then sharply decreases. However, as Maciel *et al.* (2018) demonstrated, it is not a valid pressure gradient parameter for TBLs with large velocity defect. Parameter β_{ZS} , which represents the local impact of the pressure gradient on the boundary layer regardless of velocity defect (Maciel *et al.* 2018), increases near the flow entrance up to 0.35, and then decreases to approximately 0.05 and remains mostly the same in the last part of the domain. The rapid increase of β_{ZS} at the beginning of the domain causes the increase in momentum loss in the boundary layer (H increases; figure 1c). The subsequent decrease of β_{ZS} over most of the domain should lead theoretically to momentum gain in the boundary layer (H decreases). However, because the boundary layer responds with a delay to the pressure force evolution, the momentum gain occurs only at the end of the domain.

The effect of the pressure gradient on the flow is also seen in the development of the skin friction coefficient C_f , as shown in figure 1(c); C_f decreases steadily until around $x/\delta_{av} \approx 20$, and becomes very close to zero. The behaviour of C_f and H reflects the strong non-equilibrium nature of the current APG TBL flow.

Figure 1(d) shows the spatial development of δ , δ^* and momentum (θ) thicknesses. They all increase until close to the end of the domain. Figure 1(e) shows the distributions of the most commonly used Reynolds numbers for TBLs, Re_θ and Re_τ ; Re_θ increases approximately from 2000 to 8000. The Reynolds number based on u_τ , Re_τ , develops irregularly in the streamwise direction. However, it is not valid because u_τ is not a valid scale for APG TBLs with large velocity defect. The irregularity of Re_τ stems from utilizing u_τ as a velocity scale.

2.2. Existing databases

Because we focus on spectral analysis in the current paper, we have two criteria for selecting existing databases of ZPG TBLs and channel flows: sufficiently high Reynolds number and availability of spectral distributions of Reynolds stresses, production and pressure-strain. The DNS database of Lee & Moser (2015) with $Re_\tau = 2000$ is employed for channel flows. This database is chosen because some one-dimensional (1-D) and two-dimensional (2-D) spectra are available as functions of streamwise and spanwise wavenumbers (k_x , k_z) and y . The DNS database of Sillero *et al.* (2013) with $Re_\theta = 6500$ and the experimental database of Baidya *et al.* (2021) with $Re_\theta = 6191$ are chosen for

| Name | Type | Database | Re_θ | Re_τ | H | $C_f \times 10^{-3}$ | β_{ZS} | β_{RC} | Colours & symbols |
|------|---------|----------|-------------|-----------|------|----------------------|--------------|--------------|-------------------|
| APG1 | APG TBL | DNS | 3005 | 646 | 1.65 | 2.1719 | 0.30 | 4.5 | — |
| APG2 | APG TBL | DNS | 4395 | 593 | 2.00 | 1.0674 | 0.17 | 13.6 | - - - |
| APG3 | APG TBL | DNS | 5787 | 460 | 2.63 | 0.3599 | 0.08 | 40.1 | - · - · |
| ZPGa | ZPG TBL | DNS | 6500 | 1990 | 1.35 | 2.7063 | ≈ 0 | ≈ 0 | — |
| ZPGb | ZPG TBL | Exp. | 6191 | 2493 | 1.35 | 2.7602 | ≈ 0 | ≈ 0 | ○ |
| CH | Channel | DNS | NA | 1995 | NA | 3.3605 | NA | NA | — |

Table 1. Information about the databases used in the paper: ZPGa, ZPGb, and CH indicate the databases of Sillero *et al.* (2013), Baidya *et al.* (2021) and Lee & Moser (2019), respectively.

ZPG TBLs. We chose these two databases for ZPG TBLs because the Reynolds numbers are similar and the 1-D spectral distributions of Reynolds stress and production are available as functions of k_z and y for the database of Sillero *et al.* (2013), and k_x and y for the database of Baidya *et al.* (2021). They complement each other for the spectral analysis without introducing any significant Reynolds number effect.

2.3. Flow description

We aim to investigate a wide range of velocity defect cases in this study. Three streamwise positions from the APG TBL are employed. These streamwise positions, as shown in figure 1, represent three velocity defect cases, and their corresponding shape factors are 1.65, 2.00 and 2.63. The shape factor is 1.35 for both ZPG TBL cases since they are at similar Reynolds numbers. The velocity defect is smaller in the ZPG TBL than the small-defect case of the APG TBL. As for the channel flow, the velocity defect, which is with respect to the centreline velocity, is smaller than values for the ZPG TBLs as it is well-known. These five flow cases, details of which are provided in table 1, cover a wide range of velocity defect situations, from a channel flow to a TBL with a large velocity defect.

Regarding the Reynolds numbers of the cases, the ZPG TBL and the channel flow cases have similar Re_τ and are selected at higher Re_τ and Re_θ than the APG TBL cases. We could have chosen different databases for ZPG TBLs, or channel flows with a lower Reynolds number, instead. However, it is better to analyse canonical flows at high Reynolds number because of the elevated outer-layer activity in such flows (Hutchins & Marusic 2007a). In this manner, we can compare the outer peaks of the spectral distributions of canonical flows and APG TBLs.

Throughout the paper, the streamwise, wall-normal and spanwise directions are referred to as x , y and z , or 1, 2 and 3 for index notation. The corresponding instantaneous velocity components are \bar{u} , \bar{v} and \bar{w} . The brackets $\langle \cdot \rangle$ denote ensemble averaging. Furthermore, uppercase and lowercase letters denote the mean value and the fluctuations, respectively. Thus $\langle \bar{u}_i \rangle = U_i$ and $\bar{u}_i = U_i + u_i$. The upper index + means the friction-viscous scales, with the friction velocity u_τ as the velocity scale, and ν/u_τ as the length scale.

3. Wall-normal distributions of mean flow and Reynolds stress properties

In this section, we will first investigate the wall-normal distributions of the mean flow, Reynolds stresses and Reynolds stress budgets. For all the figures presented here, profiles are plotted using a logarithmic axis for y^+ and a linear one for y/δ to examine inner

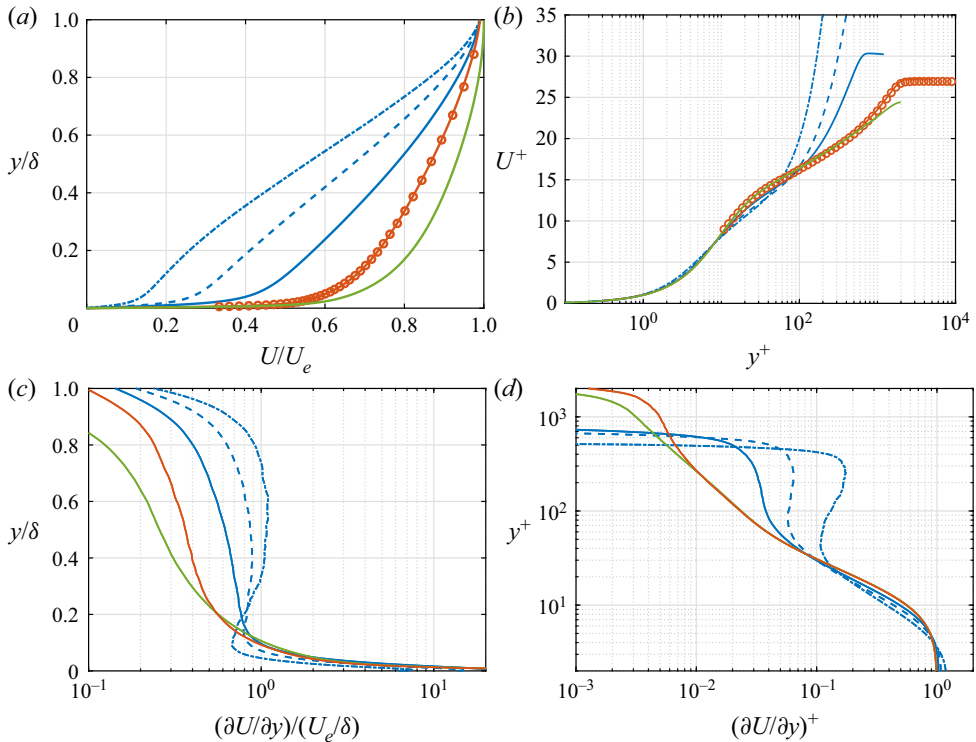


Figure 2. The mean velocity profiles of all databases normalized with (a) outer scales and (b) friction-viscous units, plus the mean shear profiles of the DNS databases normalized with (c) outer scales and (d) friction-viscous units. Legend as in table 1.

and outer layers in more detail. Furthermore, the parameters in the inner-scaled profiles are normalized using friction-viscous scales. Although friction-viscous scales are not appropriate scales for the large-defect case, they are still employed to use only one set of inner scales for simplicity. The edge velocity (U_e) and δ are employed to scale the parameters in the outer region.

3.1. Mean flow

Figures 2(a,b) present the outer- and inner-scaled mean velocities as functions of y for all the databases. The outer-scaled mean velocity profiles demonstrate the momentum deficit in the APG TBL cases. As the flow develops under the effect of the APG, the defect in the mean velocity profile increases. The profile starts to resemble velocity profiles of mixing layers (Gungor *et al.* 2016) in the large-defect case, with an inflection point in the middle of the boundary layer. The inner-scaled mean velocity profiles show that the mean velocity deviates from the log law in the APG TBL cases. Moreover, this deviation increases with increasing velocity defect. Furthermore, friction-viscous scales progressively fail to scale the mean velocity in the inner region as the defect increases (Gungor *et al.* 2016; Maciel *et al.* 2018).

Figures 2(c,d) show the mean shear profiles for the DNS databases. The mean shear profile for the experimental ZPG TBL case is not given here due to lack of points near the wall. The mean shear distribution is important because it plays a role directly in turbulence

Production and inter-component redistribution of turbulence in APG TBL

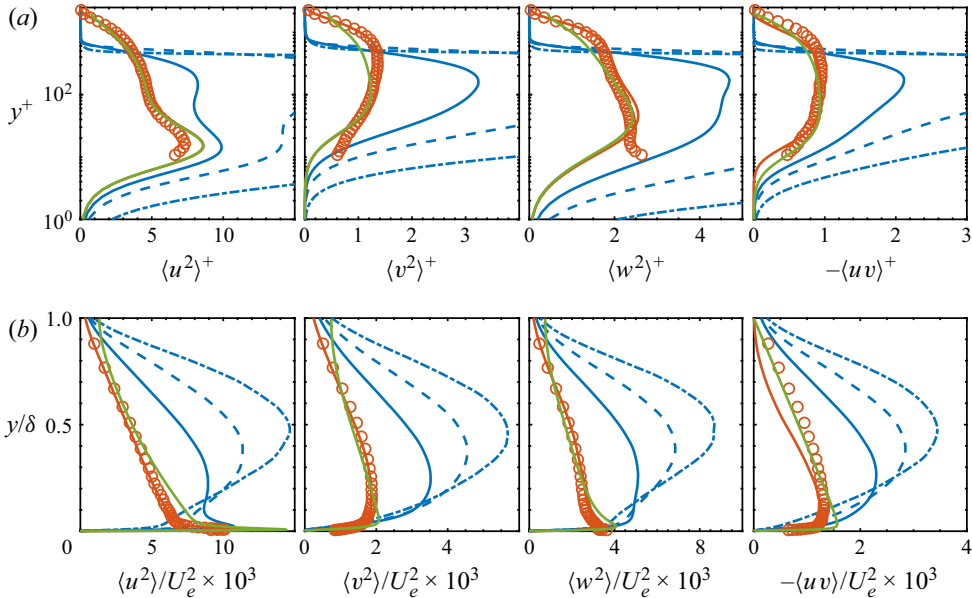


Figure 3. Reynolds stress profiles normalized with (a) friction-viscous units and (b) outer scales. Legend as in table 1.

production and hence turbulence in the flow. The change in the mean velocity profiles significantly affects the mean shear distribution in the outer layer. As the defect increases, the mean shear increases in the outer layer. More importantly, the relative magnitude of mean shear in the outer layer with respect to the inner layer increases with increasing velocity defect, as can be seen in figure 2(d). Regarding the inner layer, the mean shear remains fairly similar when it is normalized with friction-viscous scales, as expected, despite the direct effect of the pressure force near the wall in the APG TBL cases. The impact of the varying mean shear on turbulence will be discussed further in § 5.

3.2. Reynolds stresses

Figure 3 presents the wall-normal distribution of the components of the Reynolds stress tensor for all cases. The inner scales scale the Reynolds stresses well for the canonical flows. The $\langle u^2 \rangle$ profiles of the channel flow and ZPGa collapse perfectly with friction-viscous units, as expected. The $\langle u^2 \rangle$ levels are slightly smaller in ZPGb than in ZPGa in the inner layer, but this is due to the lack of spatial resolution of the probe used in the experiments (Baidya *et al.* 2017).

The change in the mean shear in the APG TBL (figures 2c,d) changes the Reynolds stress profiles progressively. The $\langle u^2 \rangle$ profiles are still fairly similar for APG1 and canonical wall-bounded flows in the inner layer, even if the scaled amplitude increases. The inner peak for $\langle u^2 \rangle$ still exists in APG1. However, such a similarity is not encountered for the other components of the Reynolds stress tensor. Moreover, figure 3(b) shows that the turbulent activity in the inner layer diminishes with respect to that in the outer layer as the defect increases. The outer layer becomes dominant as the mean shear increases in the outer layer. In the large-defect cases, APG2 and APG3, all components peak in the middle of the boundary layer, where the mean shear has a plateau. Regarding the magnitude of

the Reynolds stresses, the levels increase progressively with increasing velocity defect when Reynolds stresses are normalized with friction-viscous scales because they are not appropriate scales for large velocity defect cases (Maciel *et al.* 2018). It is important to state that U_e is not necessarily an appropriate outer scale either (Maciel, Rossignol & Lemay 2006a); however, it conserves the order of magnitude of Reynolds stresses in the range of velocity defects and Reynolds numbers of the cases examined here.

The Reynolds stress profiles of the current APG TBL case are consistent with APG TBL cases in the literature. In the small-defect case, there is an inner peak for $\langle u^2 \rangle$ and an elevated outer layer activity for all Reynolds stress components. This has been reported for equilibrium (Skåre & Krogstad 1994; Lee 2017) and non-equilibrium (Gungor *et al.* 2016) cases in small-defect APG TBLs. Moreover, the y -position and energy levels of the inner peak match well when the velocity defects of the cases are similar (Kitsios *et al.* 2016; Tanarro *et al.* 2020). Regarding the large-defect case, other researchers have already reported the increasing importance of the outer layer as the mean shear increases in the outer layer (Skåre & Krogstad 1994; Gungor *et al.* 2016; Kitsios *et al.* 2017).

3.3. Reynolds stress budgets

To understand the energy transfer mechanisms in APG TBLs, the budget of the Reynolds stress tensor is investigated first through the transport equations for the Reynolds stresses:

$$\begin{aligned}
 0 = & - \left(\langle u_i u_k \rangle \frac{\partial U_j}{\partial x_k} + \langle u_j u_k \rangle \frac{\partial U_i}{\partial x_k} \right) - \frac{\partial \langle u_i u_j u_k \rangle}{\partial x_k} \\
 & + \left\langle \frac{p}{\rho} \left(\frac{\partial u_i}{\partial x_j} + \frac{\partial u_j}{\partial x_i} \right) \right\rangle - \frac{1}{\rho} \frac{\partial}{\partial x_k} (\langle u_i p \rangle \delta_{jk} + \langle u_j p \rangle \delta_{ik}) \\
 & - 2\nu \left\langle \frac{\partial u_i}{\partial x_k} \frac{\partial u_j}{\partial x_k} \right\rangle + \nu \nabla^2 \langle u_i u_j \rangle - U_k \frac{\partial \langle u_i u_j \rangle}{\partial x_k}. \tag{3.1}
 \end{aligned}$$

Here, ν is viscosity and δ_{ik} is the Kronecker delta function. In order, the terms are production, turbulent transport, pressure-strain, pressure transport, viscous dissipation, viscous transport and mean convection.

Figure 4 presents Reynolds stress budgets for canonical flows, and small- and large-defect APG TBLs. The profiles are plotted with logarithmic and linear axes to emphasize inner and outer layer, as mentioned before. The Reynolds stress budget distributions show that energy follows the same main path in both inner and outer layers, regardless of the flow, as expected. Energy is extracted from the mean flow through $\langle u^2 \rangle$ production. Some of this energy is transferred to $\langle v^2 \rangle$ and $\langle w^2 \rangle$ through pressure-strain, which is a sink term for $\langle u^2 \rangle$ and a source term for the other normal components except in the very near-wall region. Energy is also transported or dissipated in all components. Furthermore, $\langle v^2 \rangle$ production, which is zero for channel flows and negligible for ZPG TBLs, is a sink term that transfers energy back to the mean flow in the outer region for APG TBLs. Regarding the Reynolds shear stress, the production and pressure-strain are almost in balance in all cases except in the near-wall region.

The magnitudes of the budget terms are very similar for CH and ZPGa for the inner-scaled profiles. However, the levels increase drastically as the defect increases when normalized with u_τ , consistently with the trend that we observe in the Reynolds stress profiles, which again confirms that u_τ is not a proper inner scale for APG TBLs with large velocity defect.

Production and inter-component redistribution of turbulence in APG TBL

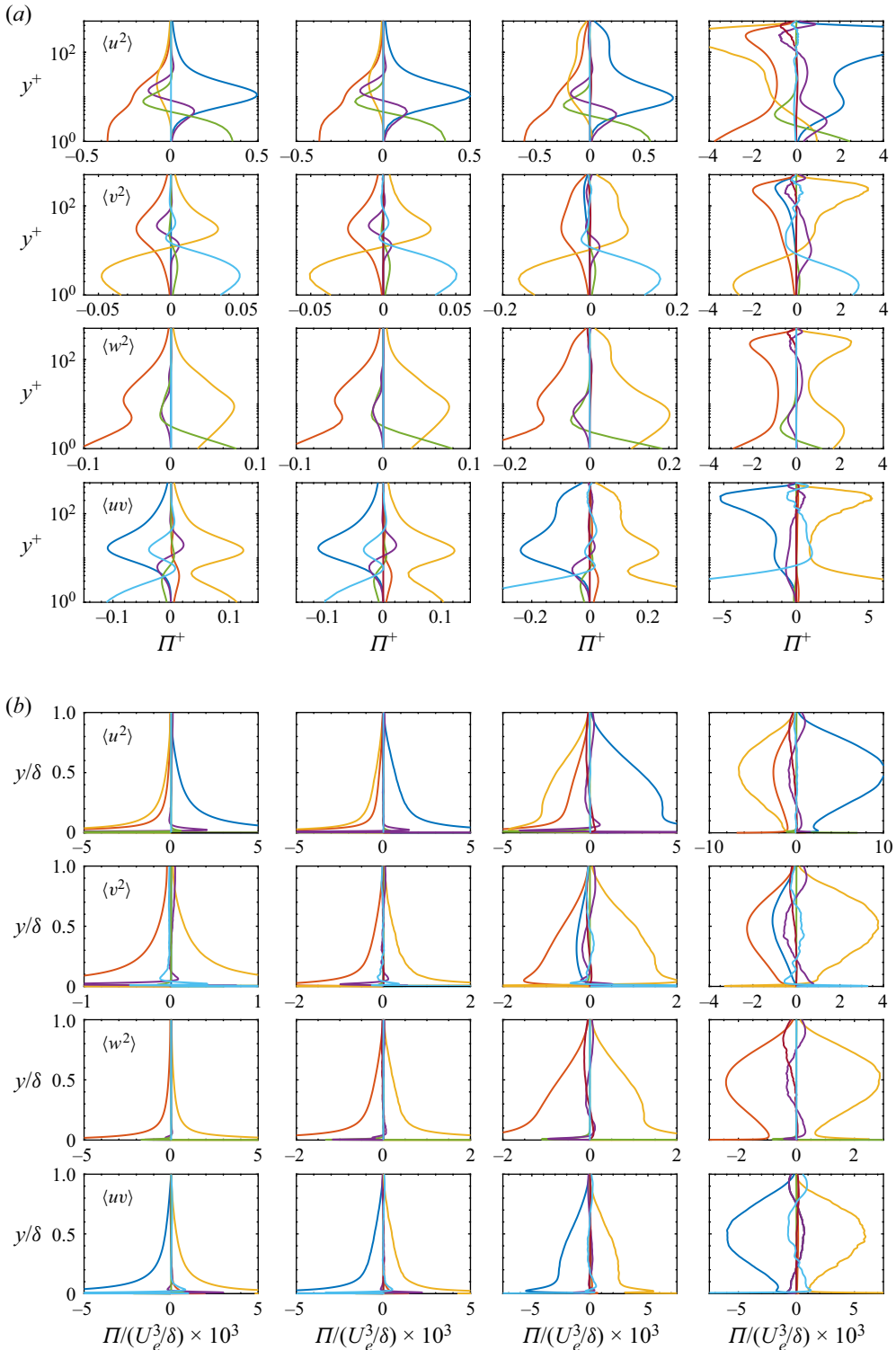


Figure 4. The Reynolds stress budgets. The levels and axes are normalized with (a) the friction-viscous scales and (b) outer scales. The rows are for $\langle u^2 \rangle$, $\langle v^2 \rangle$, $\langle w^2 \rangle$ and $\langle uv \rangle$ for each panel. Production, dark blue solid line; dissipation, red solid line; pressure-strain, yellow solid line; viscous diffusion, green solid line; turbulent transport, purple solid line; mean convection, brown solid line; pressure transport, blue solid line. **948 A5-11**

In the inner region, as [figure 4\(a\)](#) shows, the behaviours of the Reynolds stress budgets of the canonical flows and APG1 are almost the same for all normal components, regardless of the velocity defect. The shapes of the budget profiles are almost identical, with a minor shift in y^+ . For instance, the $\langle u^2 \rangle$ production peak is at $y^+ \approx 11$ and 9 in canonical flows and APG1, respectively. A clear difference between canonical flows and APG1 is that the turbulent and pressure transport above $y^+ \approx 10$ for $\langle v^2 \rangle$ are negligible for APG1.

As the mean shear distribution changes from APG1 to APG3, the overall behaviour of the source and sink terms (production, pressure-strain and dissipation) in the inner layer does not change considerably except for the aforementioned difference in magnitude. Besides the magnitude change, the main difference is that they start to increase with y above $y^+ = 30$ because they all peak in the outer layer, as is discussed later. The change of relative importance between the inner and outer layers affects turbulent transport, as well. It becomes a gain term for $\langle u^2 \rangle$ and $\langle v^2 \rangle$ in most of the inner layer due to the elevated turbulent activity in the outer layer of the large-defect case. This behaviour is also reported in equilibrium APG TBL cases for $\langle u^2 \rangle$ (Kitsios *et al.* 2017).

The Reynolds stress fluxes due to turbulent transport in the wall-normal direction, where the flux is $\theta_{ij} = \langle u_i u_j u_2 \rangle$, are given for ZPGa, APG1 and APG3 in [Appendix A \(figure 17\)](#). The $\langle u^2 \rangle$ flux towards the wall is below $y^+ = 11$ in ZPGa and APG1. In contrast, fluxes towards the wall start as high as $y/\delta = 0.4$ ($y^+ \approx 200$) in APG3, and for all Reynolds normal stresses. Strong turbulent transport towards the wall in the lower half of a near-equilibrium large-defect APG TBL was also reported by Skåre & Krogstad (1994).

Regarding the outer layer, as shown in the outer-scaled profiles in [figure 4\(b\)](#), production, pressure-strain and dissipation are at high levels between $y/\delta = 0.1$ and 0.3 in APG1, much like the Reynolds stresses themselves, but no peak is present in the outer layer. Despite the lack of an outer peak in APG1, a plateau between approximately $y/\delta = 0.1$ and $y/\delta = 0.3$ that is not observed in the channel flow and the ZPG TBL exists in production and pressure-strain terms. In the large-defect case, an outer peak emerges for the source and sink terms at around $y/\delta = 0.5$. Such a behaviour has been reported before for equilibrium (Skåre & Krogstad 1994; Kitsios *et al.* 2017) and non-equilibrium APG TBLs (Gungor *et al.* 2016).

4. Spectral analysis

The Reynolds stress and Reynolds stress budget profiles provide information about the wall-normal distributions of energy and energy transfer, but not, however, about the coherent structures that carry energy or play a role in these energy transfer mechanisms. To investigate those coherent structures, the spectral distributions of production and pressure-strain of the Reynolds stress tensor are analysed using the transport equation for the two-point velocity correlation tensor, along with the spectral distribution of energy. The reason for using the two-point correlation equation is that the spectral information is linked directly to the two-point correlations.

4.1. Methodology

We will first present the transport equation for the two-point correlation tensor. Let x_i and \tilde{x}_i be the components of the coordinates of the two points used to compute the correlations, defined as

$$\tilde{x}_i = x_i + r_i, \tag{4.1}$$

where r_i is the separation length between these points in direction i . Further, let the velocity components at x_i and \tilde{x}_j be u_i and \tilde{u}_j . Starting from the Navier–Stokes equations, the transport equations of the two-point correlation tensor $R_{ij} = \langle u_i \tilde{u}_j \rangle$ can be obtained in the form

$$\begin{aligned} \left\langle \tilde{u}_j \frac{\partial u_i}{\partial t} + u_i \frac{\partial \tilde{u}_j}{\partial t} \right\rangle = & - \underbrace{\left[U_k \left\langle \tilde{u}_j \frac{\partial u_i}{\partial x_k} \right\rangle + \tilde{U}_k \left\langle u_i \frac{\partial \tilde{u}_j}{\partial \tilde{x}_k} \right\rangle \right]}_{R_{ij}^A} - \underbrace{\left[\langle \tilde{u}_j u_k \rangle \frac{\partial U_i}{\partial x_k} + \langle u_i \tilde{u}_k \rangle \frac{\partial \tilde{U}_j}{\partial \tilde{x}_k} \right]}_{R_{ij}^P} \\ & - \underbrace{\left[\langle \tilde{u}_j \frac{\partial u_k u_i}{\partial x_k} \right] + \left\langle u_i \frac{\partial \tilde{u}_k \tilde{u}_j}{\partial \tilde{x}_k} \right\rangle}_{R_{ij}^T} - \frac{1}{\rho} \underbrace{\left[\langle \tilde{u}_j \frac{\partial p}{\partial x_i} \right] + \left\langle u_i \frac{\partial \tilde{p}}{\partial \tilde{x}_j} \right\rangle}_{R_{ij}^\Pi} \\ & + \underbrace{\left[\nu \left\langle \tilde{u}_j \frac{\partial^2 u_i}{\partial x_k \partial x_k} \right\rangle + \nu \left\langle u_i \frac{\partial^2 \tilde{u}_j}{\partial \tilde{x}_k \partial \tilde{x}_k} \right\rangle \right]}_{R_{ij}^\nu}. \end{aligned} \quad (4.2)$$

The terms on the right-hand side of the equation that are labelled as R_{ij}^A , R_{ij}^P , R_{ij}^T , R_{ij}^Π and R_{ij}^ν , are advection, production, turbulent transport, pressure and viscous terms, respectively.

The transport equations need to be simplified to perform the spectral decompositions of the various terms. In this work, the correlations are computed only in the streamwise and spanwise directions. Therefore, there is no separation in the wall-normal direction (see (4.3a)). Since all the flows considered here are homogeneous in the spanwise direction, the derivative of the mean velocity with respect to x_3 and the mean velocity in x_3 are zero (see (4.3b)). Finally, u_i is independent of \tilde{x}_α since u_i is the velocity component at another location, and this is valid for \tilde{u}_i and x_α , too. Thus their corresponding derivatives are zero (see (4.3c)). We have

$$\tilde{x}_2 = x_2, \quad (4.3a)$$

$$\frac{\partial U_i}{\partial x_3} = U_3 = 0, \quad (4.3b)$$

$$\frac{\partial u_i}{\partial \tilde{x}_\alpha} = \frac{\partial \tilde{u}_j}{\partial x_\alpha} = 0, \quad \alpha = 1, 2, 3. \quad (4.3c)$$

We need to write (4.2) as a function of separation lengths, r_1 and r_3 , to obtain the spectral distributions. Therefore, we need to substitute the independent variables x_i and \tilde{x}_i . As is usually done, the second substitution variable (associated with r_i) is chosen as the average position of the two points:

$$\Gamma_\alpha = (\tilde{x}_\alpha + x_\alpha)/2, \quad \alpha = 1, 3. \quad (4.4)$$

Let Φ be any type of two-point correlation in (4.2). We have the relationships

$$\frac{\partial \Phi}{\partial \Gamma_3} = 0, \quad (4.5a)$$

$$\frac{\partial \Phi}{\partial \Gamma_1} \approx 0, \quad (4.5b)$$

because the term $\partial\Phi/\partial\Gamma_3$ is zero due to spanwise homogeneity (see (4.5a)), and the two-point correlations are assumed to vary slowly in the streamwise direction in the case of the TBLs (see (4.5b)). The latter assumption is strong in the case of the non-equilibrium APG TBL, but it is necessary to perform the spectral decompositions. Then we perform the transformation for two-point correlations as shown in (4.6). Note that the transformation does not apply to the derivatives of mean velocity in (4.2) since these derivatives are assumed constant in x_1 and x_3 :

$$\frac{\partial\Phi}{\partial x_\alpha} = \frac{\partial\Phi}{\partial\Gamma_\alpha} \frac{\partial\Gamma_\alpha}{\partial x_\alpha} + \frac{\partial\Phi}{\partial r_\alpha} \frac{\partial r_\alpha}{\partial x_\alpha} = -\frac{\partial\Phi}{\partial r_\alpha}, \tag{4.6a}$$

$$\frac{\partial\Phi}{\partial \tilde{x}_\alpha} = \frac{\partial\Phi}{\partial\Gamma_\alpha} \frac{\partial\Gamma_\alpha}{\partial \tilde{x}_\alpha} + \frac{\partial\Phi}{\partial r_\alpha} \frac{\partial r_\alpha}{\partial \tilde{x}_\alpha} = \frac{\partial\Phi}{\partial r_\alpha}. \tag{4.6b}$$

Since we are interested in production and pressure-strain, we will discuss only these two terms hereafter. The production term in (4.2) can be rewritten by taking advantage of (4.3a) and (4.3b):

$$R_{ij}^P = -\langle \tilde{u}_j u_1 \rangle \frac{\partial U_i}{\partial x_1} - \langle u_i \tilde{u}_1 \rangle \frac{\partial \tilde{U}_j}{\partial \tilde{x}_1} - \langle \tilde{u}_j u_2 \rangle \frac{\partial U_i}{\partial x_2} - \langle u_i \tilde{u}_2 \rangle \frac{\partial \tilde{U}_j}{\partial \tilde{x}_2}. \tag{4.7}$$

Furthermore, by assuming that the derivatives of the mean velocity with respect to x_1 and x_2 do not change in x_1 , i.e.

$$\left. \begin{aligned} \frac{\partial \tilde{U}_k}{\partial \tilde{x}_1} &= \frac{\partial U_k}{\partial x_1}, \\ \frac{\partial \tilde{U}_k}{\partial \tilde{x}_2} &= \frac{\partial U_k}{\partial x_2}, \end{aligned} \right\}, \tag{4.8}$$

the production term can be rewritten as

$$R_{ij}^P = -\langle \tilde{u}_j u_1 \rangle \frac{\partial U_i}{\partial x_1} - \langle u_i \tilde{u}_1 \rangle \frac{\partial U_j}{\partial x_1} - \langle \tilde{u}_j u_2 \rangle \frac{\partial U_i}{\partial x_2} - \langle u_i \tilde{u}_2 \rangle \frac{\partial U_j}{\partial x_2}. \tag{4.9}$$

In addition, the derivative of the mean velocity in the streamwise direction is zero for channel flows due to the streamwise homogeneity, and is negligible in the ZPG TBLs. Therefore, the production term is simplified for the canonical flow cases as

$$R_{ij}^P = -\langle \tilde{u}_j u_2 \rangle \frac{\partial U_i}{\partial x_2} - \langle u_i \tilde{u}_2 \rangle \frac{\partial U_j}{\partial x_2}. \tag{4.10}$$

The pressure term in (4.2) is divided into two terms,

$$R_{ij}^\Pi = R_{ij}^d + R_{ij}^s, \tag{4.11}$$

where R_{ij}^d and R_{ij}^s are pressure transport and pressure-strain, respectively. By taking advantage of the relationships and mathematical manipulations introduced previously, the pressure-strain term is written for the wall-parallel, $R_{\alpha\alpha}^s$, and wall-normal, R_{22}^s , directions

as

$$R_{\alpha\alpha}^s = \frac{1}{\rho} \left\langle -p \frac{\partial u_i}{\partial r_\alpha} + \tilde{p} \frac{\partial \tilde{u}_j}{\partial r_\alpha} \right\rangle, \quad \alpha = 1, 3, \quad (4.12)$$

$$R_{22}^s = \frac{1}{\rho} \left(\left\langle \tilde{p} \frac{\partial u_i}{\partial x_2} \right\rangle + \left\langle p \frac{\partial \tilde{u}_j}{\partial \tilde{x}_2} \right\rangle \right). \quad (4.13)$$

There are several ways to perform the decomposition of the pressure term, but we chose this one for two reasons. First, we want to be consistent within the paper, because the spectral distributions of the channel flow that we use in the paper are obtained using the same decomposition as in Lee & Moser (2019). The other reason is that this decomposition is consistent with many studies in the literature (Mansour, Kim & Moin 1988; Mizuno 2016) and, more importantly, with the Reynolds stress transport equation as written in (3.1) when r_x and r_z tend to zero. In other words, by integrating the spectral distributions of these terms over the wavenumbers, the budget of the Reynolds stresses, which is discussed in the previous section, is obtained.

The spectral distributions of production and pressure-strain are obtained by performing the Fourier transform of each term with respect to r_x and r_z . In the paper, 1-D spectra are computed as functions of wavenumber component k_x or k_z , and 2-D spectra as functions of k_x and k_z . The derivation above is for the 2-D spectra, but a similar derivation is performed, albeit not given here, for the 1-D spectra.

We utilize temporal data to obtain the spectra in k_x . We invoke Taylor's frozen turbulence hypothesis to convert frequency into streamwise wavenumber

$$k_x = \frac{2\pi f}{U_c}, \quad (4.14)$$

where f is the sampling frequency, and U_c is the convection velocity, which is taken to be the local mean velocity.

In the paper, the spectra are always plotted as pre-multiplied by the wavenumbers, and the wavenumber axes are always in logarithmic scale. For 1-D spectra, the wall-normal axis is plotted in linear scale for the outer layer and logarithmic scale for the inner layer, so that both layers are examined in a more detailed, clear way.

The premultiplied 1-D spectral distributions of energy (shaded), production (red) and pressure-strain (purple) as functions of y and wavelength components λ_x and λ_z for all components of the Reynolds stress tensor are presented using friction-viscous scales in figure 5. In addition, the outer-scaled spectral distributions are given in figure 18 in Appendix B. The 1-D pressure-strain spectra are available only for the APG TBL cases. Furthermore, $\langle v^2 \rangle$ production is plotted only for the APG TBL cases due to the fact that it is zero for channel flows and negligible for ZPG TBLs.

4.2. Energy

We start by discussing the energy spectra (shaded contours) of the channel flow and ZPG TBLs. The spectral distribution of energy shows that energy-carrying structures are found mainly in the inner layer in the channel flow and ZPG TBLs, with some activity in the outer layer. A strong peak is located at $\lambda_z^+ \approx 120$ and $\lambda_x^+ \approx 1000$ in the inner layer for the $\langle u^2 \rangle$ spectra. It is associated with the well-known streamwise streaks in the near-wall region of canonical wall-bounded flows. As for the outer layer, the $\langle u^2 \rangle$ and $\langle uv \rangle$ distributions show an outer peak in the spanwise spectra. The streamwise spectra of CH and ZPGb do

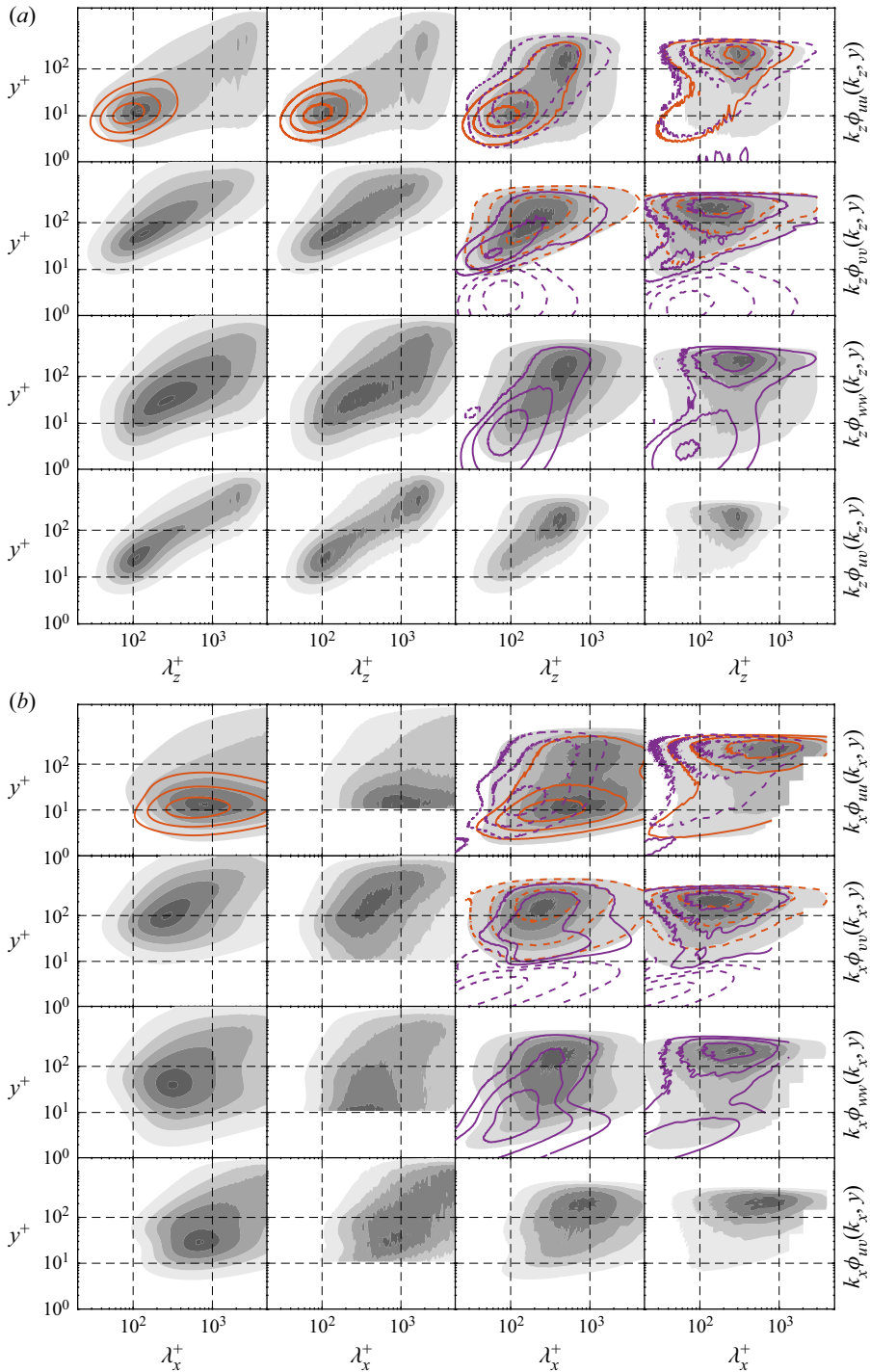


Figure 5. The premultiplied 1-D energy (shaded contours), production (red contours) and pressure-strain (purple contours) spectra of the channel flow (first column), the ZPG TBLs (second column), APG1 (third column), and APG3 (fourth column) as functions of (a) λ_z^+ and (b) λ_x^+ , and y^+ . The rows in each panel are respectively $\langle u^2 \rangle$, $\langle v^2 \rangle$, $\langle w^2 \rangle$ and $\langle uv \rangle$. The contour levels are [0.1 0.3 0.5 0.7 0.9] of the maxima of spectra for energy, and [0.3 0.7] of the maxima of spectra for production and pressure-strain. The dashed contours indicate negative values. The horizontal and vertical dashed lines indicate $y^+ = 10, 100$ and $\lambda^+ = 100, 1000$.

not exhibit a clear outer peak because Re_τ is not high enough. Channel flows and ZPG TBLs with higher Re_τ have a distinct outer peak in their streamwise spectra (Hutchins & Marusic 2007b; Mathis *et al.* 2009). This increased outer layer activity in canonical flows, as mentioned before, is attributed to the elongated meandering motions in the outer layer (Marusic *et al.* 2010a).

The energy spectra in the small-defect case of the APG TBL, APG1, demonstrate an intense turbulent activity in both inner and outer layers. The relative importance of the turbulent activity in the outer layer with respect to the inner layer is higher in APG1 than in the canonical flows. As streamwise and spanwise spectra show, energetic $\langle u^2 \rangle$ -carrying structures are more streamwise elongated and streaky in the inner layer than in the outer layer, and the most energetic outer layer structures are slightly longer in the streamwise direction. The situation is different for the other Reynolds stress components. Even though there is energy in the inner layer, the inner peak vanishes in the streamwise and spanwise spectra. In the outer layer, whereas $\langle uv \rangle$ -carrying structures have streamwise lengths similar to $\langle u^2 \rangle$ -carrying ones, the $\langle v^2 \rangle$ - and $\langle w^2 \rangle$ -carrying structures are shorter. Similar findings were reported for channel flows by Jiménez & Hoyas (2008).

The most energetic $\langle u^2 \rangle$ structures in the inner layer of APG1 are at $y^+ = 15$ with λ_z^+ of 120 and λ_x^+ of approximately 650, as seen from figure 5. The spanwise wavelength and the wall-normal location are the same as in the channel flow and the ZPG TBL. This indicates that the wall-normal position and width of the most energetic structures are not affected by relatively small velocity defects. Similar values for λ_z^+ and y^+ of the inner peak have been reported in the literature for non-equilibrium (Tanarro *et al.* 2020) and near-equilibrium (Lee 2017; Bobke *et al.* 2017) APG TBL cases with small velocity defect, with shape factors varying from 1.42 to 1.74. Despite the similarity of the wall-normal position and λ_z^+ of the inner peak, its streamwise wavelength is smaller in APG1 than in the canonical cases, where the inner peak is at $\lambda_x^+ = 800$ in CH and approximately at 1000 in ZPGb. There are conflicting findings about λ_x^+ of the inner peak in APG TBLs in the literature. A reduction of λ_x^+ like in the present APG TBL has been reported by Sanmiguel Vila *et al.* (2020a) in their TBL cases, with shape factors varying from 1.31 to 1.51 as the defect increases. However, no decrease was observed by Harun *et al.* (2013) in their APG TBL case, with a shape factor of 1.41 with respect to their ZPG and favourable pressure gradient TBLs.

In the large-defect case, APG3, figure 5 shows that turbulent activity becomes much weaker in the inner layer than in the outer layer. The inner peak in the energy spectra of $\langle u^2 \rangle$ vanishes completely. Furthermore, the shape of the spectra of $\langle u^2 \rangle$ is different from the other flow cases. For instance, the energy found in the inner layer is at large wavelengths. This suggests that the large-scale outer-layer structures might strongly influence the inner layer in the large-defect case. Although not seen clearly in figures 5 and 18, this near-wall footprint of the large-scale structures actually appears to increase from ZPG to APG3, as the line representation of 1-D spectra reveals (not shown here). Harun *et al.* (2013) have reported that the near-wall footprint increases as pressure gradient is increased from favourable to adverse – note that they considered only a small-defect APG case comparable to APG1. For the other Reynolds stress components, the trend of the inner layer losing its importance with respect to the outer layer continues as the defect increases from APG1 to APG3.

That the outer-layer large-scale structures become dominant in large-defect APG TBLs was also reported for equilibrium flows. Lee (2017) showed that the inner peak of the spanwise energy spectra of $\langle u^2 \rangle$ is absent in an equilibrium APG TBL with $H = 1.98$, whereas it still exists when the shape factor is 1.76. Moreover, Kitsios *et al.* (2017) also

showed that the $\langle u^2 \rangle$ spectra do not exhibit an inner peak in their near-equilibrium APG TBL case with a large velocity defect ($H = 2.35$). These studies suggest that the general trend of the spectral behaviour of $\langle u^2 \rangle$ -carrying structures are similar in large-defect APG TBLs regardless of the upstream history of flow.

The structures carrying most of the Reynolds stresses are found predominantly in the outer layer in APG3, in the middle of the boundary layer, as shown in more detail in [figure 18](#) in [Appendix B](#). The situation is the same for all components. Regarding their shape, $\langle u^2 \rangle$ -carrying structures are more streamwise elongated than those carrying the other components. In addition, $\langle u^2 \rangle$ -carrying structures are the longest structures with a λ_x of 2δ . The most energetic structures have approximately the same λ_z , namely, 0.75δ , except $\langle v^2 \rangle$ -carrying ones with $\lambda_z = 0.25\delta$. The prominent distinction between APG3 and APG1 is that energetic structures are located in $y/\delta = 0.4\text{--}0.6$ in APG3 and $y/\delta = 0.15\text{--}0.3$ in APG1. Moreover, the shape of the 1-D energy spectra of $\langle u^2 \rangle$ is different between the two defect cases, which happens due to the intense inner-layer activity in APG1.

To give a more complete picture of spectral properties of the energetic structures, [figure 6](#) presents the outer 2-D spectral distributions of energy for CH, APG1 and APG3 as functions of λ_x/δ and λ_z/δ at several wall-normal locations (2-D spectra are not available for the ZPG TBL). The $\langle u^2 \rangle$ - and $\langle uv \rangle$ -carrying structures, especially the most energetic ones, are streaky and streamwise elongated in all flows, but they are more streamwise elongated in the channel flow than in the APG TBL cases. For instance, the peak for $\langle u^2 \rangle$ spectra is at $\lambda_x \approx 7\delta - 9\delta$ in channel flows, but it is at $\lambda_x \approx 2\delta$ in the APG TBL cases. This difference can be attributed to the presence of very-large-scale structures in channel flows, which become important in high-Reynolds-number flows (Marusic *et al.* 2010b). In contrast, $\langle v^2 \rangle$ - and $\langle w^2 \rangle$ -carrying structures are not streamwise elongated. The highest contours of the energy spectra for $\langle v^2 \rangle$ and $\langle w^2 \rangle$ tend to follow the linear relationship $\lambda_z \sim \lambda_x$ in all cases, even though structures are smaller in the APG TBL cases.

The energetic structures do not vary with y in the outer layer as the defect increases. In the channel flow, the smallest defect case, the shapes of the 2-D spectra remain similar as y increases, but the sizes of the structures increase with respect to δ for all components. The situation is similar in APG1, but with smaller size variations. In the large-defect case, the shapes of the 2-D spectra and the sizes of the structures remain almost identical starting from $y/\delta = 0.1$. This trend happens probably because of increasing outer-layer activity as the mean shear increases in the outer layer. As the outer-layer large-scale structures start dominating the flow and the effect of the inner layer decreases, the structures that carry most of the energy have very similar spectral features in the outer layer.

Regarding the absolute levels of the spectral distributions (not shown in [figure 5](#) since relative levels are used), they increase when they are normalized with u_τ and U_e . This is consistent with the change of Reynolds stress profiles levels with increasing velocity defect as discussed in [§ 3.2](#).

4.3. Production

After discussing the energy spectra, we continue with production spectra to understand the behaviour of turbulence-producing structures. The $\langle u^2 \rangle$ and $\langle v^2 \rangle$ productions are discussed separately since the former is a source term and the latter is a sink term that is zero in channel flows and negligible in ZPG TBLs. The $\langle u^2 \rangle$ production spectra of [figure 5](#) reflect the changes that were already observed with the production profiles of [figure 4](#). Production resides mostly in the inner layer in the case of the canonical flows, in both layers for APG1,

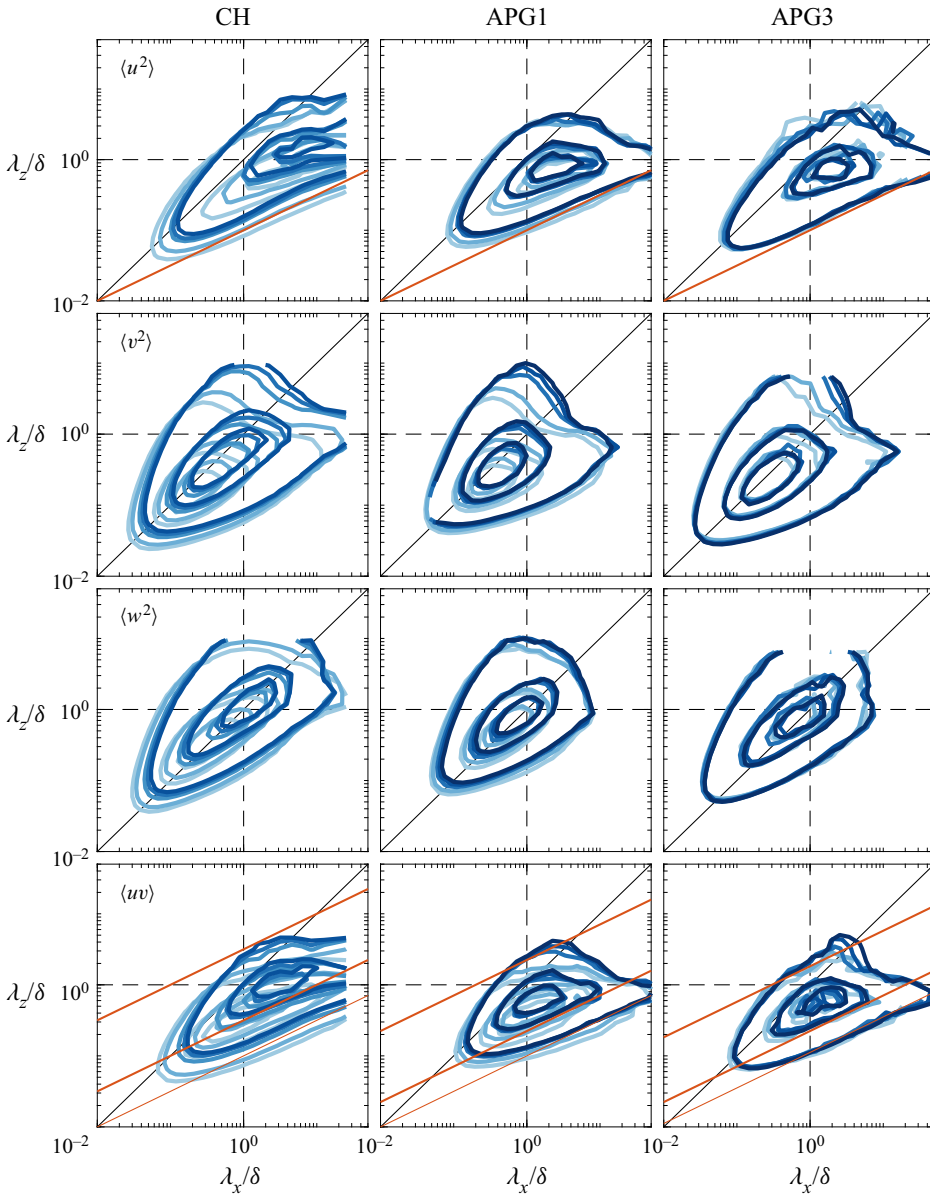


Figure 6. The premultiplied 2-D energy spectra of CH (first column), APG1 (second column) and APG3 (third column) as functions of λ_z/δ and λ_x/δ for $y/\delta = [0.1 \ 0.15 \ 0.3 \ 0.4 \ 0.5]$. The colour is darker as y increases. The rows are for $\langle u^2 \rangle$, $\langle v^2 \rangle$, $\langle w^2 \rangle$, and $\langle uv \rangle$. The contour levels are $[0.1 \ 0.5 \ 0.8]$ of the maxima of spectra at each wall-normal position. The black solid and dashed lines indicate $\lambda_x = \lambda_z$ and $\lambda_{x,z} = \delta$, respectively; the red lines indicate $\lambda_z \sim \lambda_x^{1/2}$.

and mostly in the outer region for APG3. The detailed characteristics of the $\langle u^2 \rangle$ production spectra in the inner and outer layers are discussed at length in § 5.

Figure 7 shows the premultiplied 2-D production spectra for the $\langle u^2 \rangle$ component as a function of λ_x/δ and λ_z/δ for several wall-normal locations of CH, APG1 and APG3. Note that the $\langle uv \rangle$ spectra (figure 6, bottom row) and the $\langle u^2 \rangle$ production spectra have

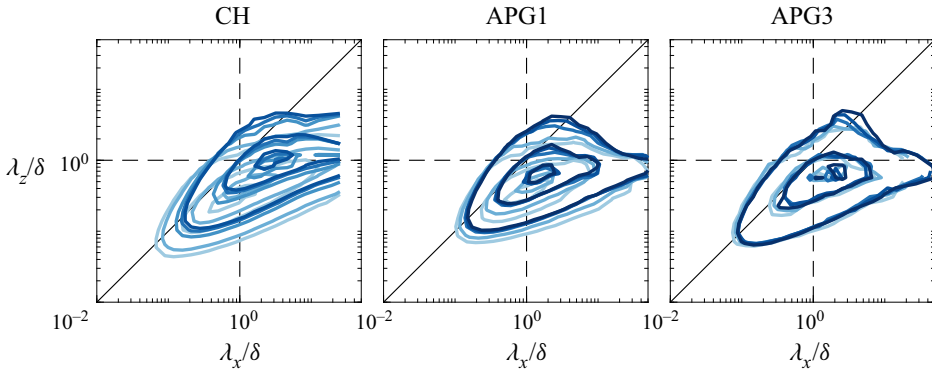


Figure 7. The premultiplied 2-D production spectra of $\langle u^2 \rangle$ of CH (first column), APG1 (second column) and APG3 (third column) as functions of λ_z/δ and λ_x/δ for $y/\delta = [0.1 \ 0.15 \ 0.3 \ 0.4 \ 0.5]$. The colour is darker as y increases. The contour levels are $[0.1 \ 0.5 \ 0.9]$ of the maxima of spectra at each wall-normal position. The straight and dashed lines indicate $\lambda_x = \lambda_z$ and $\lambda_{x,z} = \delta$, respectively.

similar features because the spectral density function of $\langle uv \rangle$ is dominant in the production spectrum. This can be deduced from the two-point-correlation production term of (4.9) with $i = j = 1$. The resemblance is especially strong in the case of the channel flow where production involving $\partial U/\partial x$ is zero (4.10). The production structures are streaky and streamwise elongated in all cases. The shapes of the spectra are similar in all cases, but with smaller structures for the APG TBLs. Whereas the streamwise–spanwise characteristics change with y in the channel flow and APG1 to a lesser extent, they remain the same in the large-defect case, as happens for the energy spectra of figure 6.

Regarding $\langle v^2 \rangle$ production, as was seen from the profiles in figure 4, it is zero in channel flow, negligible in the ZPG TBL cases, and negative in the APG TBL cases. It is found in the outer layer of both APG TBL cases, and it becomes more important with increasing velocity defect, as was mentioned previously. The spectral distributions of figure 5 show that the $\langle v^2 \rangle$ production spectra are very similar to the $\langle v^2 \rangle$ energy spectra.

4.4. Inter-component energy transfer

After analysing the turbulence-producing structures, the pressure-strain spectra, as shown in figure 5 with purple contours, are analysed to understand the characteristics of structures that are active in inter-component energy transfer. Note that 1-D pressure-strain spectra are not available for the canonical flows. However, 2-D pressure-strain spectra are accessible for the channel flow, and are discussed further below. As discussed previously in § 3, pressure-strain governs the inter-component energy transfer. Since turbulence is transferred mostly from $\langle u^2 \rangle$ to $\langle v^2 \rangle$ and $\langle w^2 \rangle$, the $\langle u^2 \rangle$ component of the pressure-strain is negative, and the other components are positive throughout the boundary layer, excluding the very-near-wall region where the $\langle v^2 \rangle$ component is negative for both defect cases.

In the inner layer, as streamwise and spanwise spectra (figure 5) present, most of the inter-component energy transfer takes place with small-scale structures. In the small-defect case, $\langle u^2 \rangle$ transfers energy from structures wider than those that receive it for $\langle v^2 \rangle$ and that are above those that receive it for $\langle w^2 \rangle$. The pressure-strain structures' lengths are shorter

than most energetic structures, and the structures are less streaky. The pressure-strain spectra are qualitatively similar in the small-defect case of the APG TBL and the channel flow of Lee & Moser (2019). In the large-defect case, there is still some pressure-strain in the inner layer, as happens with production, even though most of the inter-component energy transfer takes place in the outer layer.

Indeed, the inter-component energy transfer becomes dominant in the outer layer and is driven by large-scale structures as the mean shear increases in the outer layer, as can be seen in figure 5. This is consistent with the behaviour of energetic and production structures. The energy is transferred from $\langle u^2 \rangle$ to $\langle v^2 \rangle$ and $\langle w^2 \rangle$ at similar wall-normal positions for all components, unlike what happens in the inner layer. Whereas the spanwise wavelength of energy transferring outer layer $\langle u^2 \rangle$ and $\langle w^2 \rangle$ structures are the same, $\langle v^2 \rangle$ structures are slightly narrower. The spanwise wavelengths and wall-normal positions where most of the energy transfer takes place are like those of $\langle u^2 \rangle$ production. Therefore, the outer turbulent energy is both produced and transferred to other components by structures of similar spanwise sizes and at similar locations. In the case of the streamwise length of the dominant pressure-strain structures, it is shorter than that of energetic structures for $\langle u^2 \rangle$ and almost the same for $\langle v^2 \rangle$ and $\langle w^2 \rangle$.

In the outer region, narrow structures ($\lambda_z < 0.3\delta$ in the small-defect case, and $\lambda_z < 0.15\delta$ in the large-defect case) transfer energy predominantly from $\langle u^2 \rangle$ to $\langle v^2 \rangle$. In contrast, there is no such distinction between $\langle v^2 \rangle$ and $\langle w^2 \rangle$ for wide structures. Both $\langle v^2 \rangle$ and $\langle w^2 \rangle$ receive a similar amount of energy, although the levels are not given in figure 5. That energy transfer at small scale is from $\langle u^2 \rangle$ to $\langle v^2 \rangle$ is also consistent with the fact that the energetic $\langle v^2 \rangle$ structures have shorter spanwise wavelengths than the energetic $\langle u^2 \rangle$ and $\langle w^2 \rangle$ structures, as discussed before.

Figure 8 presents the 2-D spectral distribution of pressure-strain for channel flow, APG1 and APG3 as a function of λ_x/δ and λ_z/δ for several wall-normal positions in the outer region. The structures' size notably increases in the channel flow as y increases. It increases for APG1 too, but the increase is much milder. In contrast, the spectra do not vary for APG3 throughout the outer layer, in agreement with the energy and production spectra. The shape of the spectra remains qualitatively similar for each component regardless of the velocity defect. This shows that the spectral features of the pressure-strain structures are not significantly affected by the velocity defect, but their width and length slightly decrease with increasing velocity defect.

5. Effects of the velocity defect on inner and outer layer turbulence

To better understand the effects of the velocity defect on energetic, production and pressure-strain structures, we now investigate the spectral distributions separately in the inner and outer layers because, as mentioned above, an intense activity in one layer hides what is happening in the other layer. Therefore, spectral distributions are now plotted separately for each layer using their respective maxima. Furthermore, we plot spectral distributions of energy, production and pressure-strain together because we are interested in relative size and y -positions of structures with respect to each other.

Regarding the definition of the inner and outer layers, there is no commonly accepted definition for APG TBLs (Maciel *et al.* 2018). For the current study, we intend to separate the inner and outer peaks when they exist. For this reason, we focus on the region $0 < y^+ < 60$ for the inner layer and $0.1 < y/\delta < 1$ for the outer region. Nevertheless, it is essential to state that these ranges may be specific to the flows studied here.

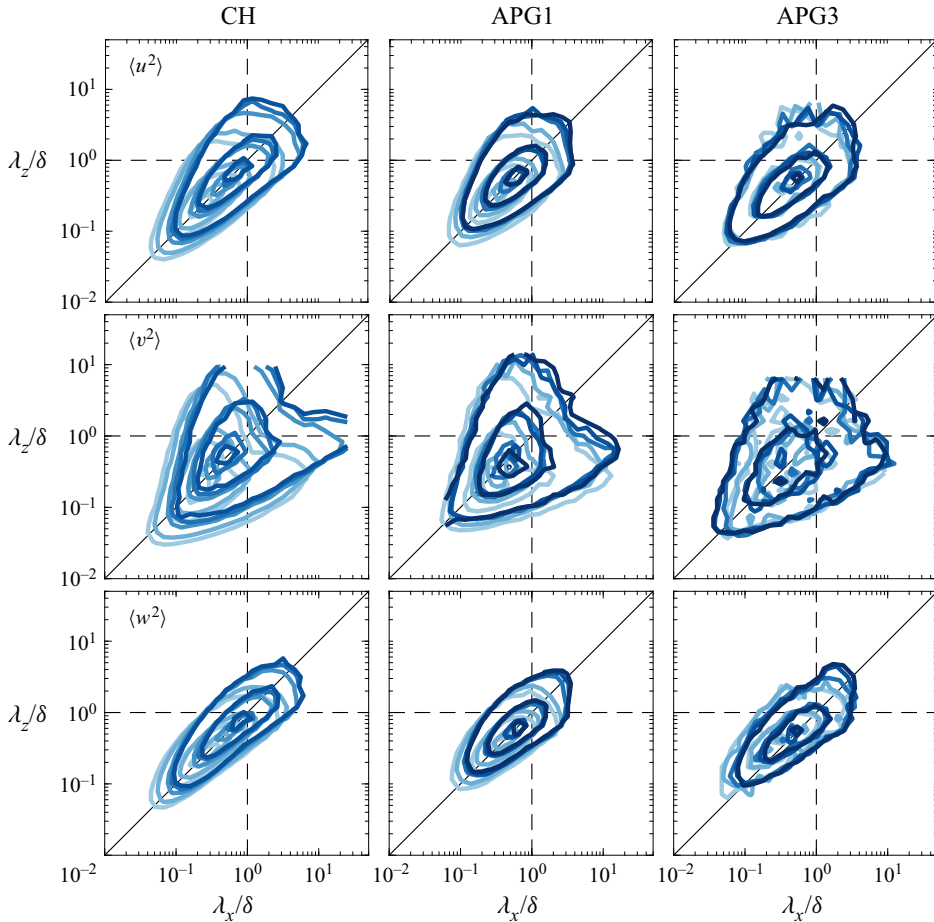


Figure 8. The premultiplied 2-D pressure-strain spectra of CH (first column), APG1 (second column) and APG3 (third column) as functions of λ_z/δ and λ_x/δ for $y/\delta = [0.1 \ 0.15 \ 0.3 \ 0.4 \ 0.5]$. The colour is darker as y increases. The rows are $\langle u^2 \rangle$, $\langle v^2 \rangle$ and $\langle w^2 \rangle$. The contour levels are $[0.1 \ 0.5 \ 0.9]$ of the maxima of spectra at each wall-normal position. The straight and dashed lines indicate $\lambda_x = \lambda_z$ and $\lambda_{x,z} = \delta$, respectively.

5.1. Inner layer

First, we investigate the inner layer of the small-defect case and compare it with the inner layers of the ZPG TBLs and channel flow. Figures 9(a,d) show the inner-scaled $\langle u^2 \rangle$ and $\langle v^2 \rangle$ production profiles in the inner layer. The parameters are normalized with their maximum in the inner layer. The profiles of $\langle u^2 \rangle$ collapse perfectly for CH and ZPGa. There is a minor mismatch for ZPGb due to a decrease in levels, as explained before. The profile of APG1 is also very similar to the profiles of the canonical flows. The peak is at $y^+ = 15$ in all cases. Regarding the $\langle v^2 \rangle$ production profiles (figure 9d), the shape is very similar in all cases. The CH and ZPGa profiles collapse perfectly again, but as the defect increases, the wall-normal position of the peak location decreases slightly from $y^+ = 11$ in canonical flows to $y^+ = 9$ in APG1.

Figures 9(b,c,e,f) present the inner-scaled energy and production spectra of $\langle u^2 \rangle$ as a function of λ^+ and y^+ for the same flows. Like the profiles of $\langle u^2 \rangle$ and $\langle v^2 \rangle$ production, the spectra of the three flows are similar in friction-viscous units, the most noticeable

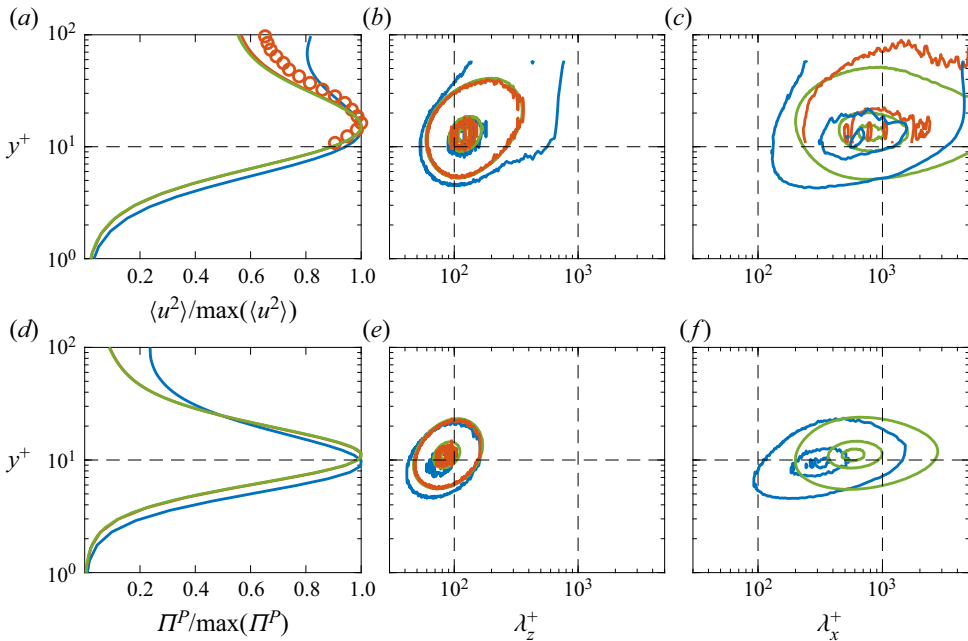


Figure 9. The (a) $\langle u^2 \rangle$ and (d) $\langle u^2 \rangle$ production profiles in the inner layer as functions of y . The levels are normalized with the maximum of each profile. The premultiplied (b,c) energy and (e,f) production spectra of $\langle u^2 \rangle$ as functions of y^+ and (b,e) λ_z^+ and (c,f) λ_x^+ for APG1, the ZPG TBLs and the channel flow. The contour levels are [0.5 0.9] of the maxima of spectra. Colours and symbol as in table 1.

difference being shorter streamwise wavelengths for APG1. The difference in streamwise wavelength is more pronounced for the production spectra (figure 9f); the production peak is at $\lambda_x^+ \approx 550$ for the channel flow and $\lambda_x^+ \approx 300$ for APG1. For the spanwise spectra (figures 9b,e), the inner peak and contours scale well for the energy and production spectra, although the production peak is located slightly below for APG1. The aforementioned similarities in profiles and spectra suggest that the $\langle u^2 \rangle$ -carrying and production structures are not affected significantly by a small increase in the velocity defect, but they are definitely shortened.

After discussing the similarities between the canonical flows and the small-defect case, we compare the small- and large-defect cases of the APG TBL in the inner layer, this time with the possibility of also comparing the pressure-strain spectra. Figure 10 presents the energy, production and pressure-strain spectra for all normal components of the Reynolds stress tensor for APG1 and APG3. It is important to state that the spectra shown in figure 10 are the same ones as in figure 5. However, in figure 10, the outer layer is hidden, and the spectra are plotted with their maximum in the inner layer to examine the inner layer in more detail, whereas figure 5 shows the spectra for the whole boundary layer. The most prominent difference between APG3 and APG1 is that the inner peak in the energy spectra of $\langle u^2 \rangle$ vanishes completely in the large-defect case. This is rather important because the inner peak of $\langle u^2 \rangle$ is partly the signature of the streaks that are an essential part of the near-wall cycle. In contrast, both production and pressure-strain spectral distributions of $\langle u^2 \rangle$ for APG3 exhibit an inner peak, although the peak is not clear because the spectra are noisy in the large-defect case. As far as the shape is concerned, the shapes of production and pressure-strain spectra of $\langle u^2 \rangle$ are similar in both APG TBL cases. Moreover, the

relative positions and dimensions of the production and pressure-strain structures do not change significantly with increasing velocity defect. The main difference between the defect cases is the y^+ -position and λ^+ of the inner peak of production and pressure-strain spectra of $\langle u^2 \rangle$. In APG3, the structures are closer to the wall, and their λ_x^+ and λ_z^+ are smaller than in APG1. As mentioned previously, this trend is expected because of the use of friction-viscous scales (Maciel *et al.* 2018). Nonetheless, the fact that the spectra remain similar indicates that the friction-viscous length is still relevant as a length scale for production and pressure-strain structures, at least for APG TBLs up to $H = 2.6$, even if there is no significant energy in the inner layer, as shown before, and structures become irregular and disorganized (Maciel *et al.* 2017b). However, the friction-viscous length cannot be a legitimate length scale in larger-defect APG TBLs considering that the friction velocity goes to zero at separation.

To complete the picture, figure 11 presents the 2-D spectra of energy, production and pressure-strain for the channel flow, APG1, and APG3 as a function of λ_x^+ and λ_z^+ at $y^+ \approx 13$, a position close to the peaks of energy and production of $\langle u^2 \rangle$. Both energetic and production structures of $\langle u^2 \rangle$ are streamwise elongated, but production structures are shorter and narrower than most energetic ones for the channel flow and the small-defect case. In addition, pressure-strain structures of $\langle u^2 \rangle$ are much shorter and less streamwise elongated than production and energetic structures. In the large-defect case, as discussed earlier, the spectra do not show any signs of the existence of streaks that are characteristic of the near-wall cycle. Whereas the peak of the energy spectrum is at $\lambda_x^+ = 700\text{--}800$ and $\lambda_z^+ = 120$ for channel flow and APG1, it is at approximately $\lambda_x^+ = 1000$ and $\lambda_z^+ = 400$ for APG3. The increase in size could be due to the fact that the outer-layer large-scale wide structures dominate the inner layer. This is consistent with the previous discussions about outer-layer structures' footprints (figure 5) and the fact that 2-D energy spectra are much more similar in APG3 in the wall-normal direction (figure 6). On the other hand, the production and pressure-strain structures of $\langle u^2 \rangle$ are shorter in APG3, but they have similar relative sizes as in CH and APG1. Furthermore, the shapes of the production and pressure-strain spectra in all cases are alike.

As for the $\langle v^2 \rangle$ component, the pressure-strain spectra have a distinctive shape in all flows. They have a second peak, weaker than the primary peak, although the peak is not clear in APG3 due to the fact that the spectrum is noisy. This peak is at the same λ_x^+ as the primary peak, but λ_z^+ is considerably higher ($\lambda_z^+ \approx 300$) than in the primary peak ($\lambda_z^+ \approx 50$). The secondary peak might indicate that two types of pressure-strain structures play a role in receiving energy for $\langle v^2 \rangle$ in the inner layer. The primary peak's λ_x^+ decreases with increasing velocity defect from $\lambda_x^+ \approx 300$ to $\lambda_x^+ \approx 150$, while its λ_z^+ increases very mildly.

The spectra for $\langle w^2 \rangle$ are alike for CH and APG1 but are different in APG3. The shapes of the spectra and the sizes of the structures do not change considerably as the defect increases from channel flow to APG1. The energetic structures are bigger than the pressure-strain structures. However, the energy spectrum for $\langle w^2 \rangle$ become drastically different for APG3, as happens for the $\langle u^2 \rangle$ spectrum. The $\langle w^2 \rangle$ -carrying structures are much broader in APG3 than in the others, but their length is similar. The peak of the energy spectra is at $\lambda_z^+ \approx 150$ for the channel flow and APG1, but at $\lambda_z^+ \approx 350$ in APG3. On the other hand, the pressure-strain structures behave in a similar fashion for $\langle v^2 \rangle$ and $\langle w^2 \rangle$. The peak of the pressure-strain spectrum is at $\lambda_z^+ \approx 100$, but λ_x^+ decreases from approximately 200 to 80 from channel flow to APG3. This behaviour is considerably different from the behaviour of the most energetic $\langle w^2 \rangle$ -carrying structures.

Production and inter-component redistribution of turbulence in APG TBL

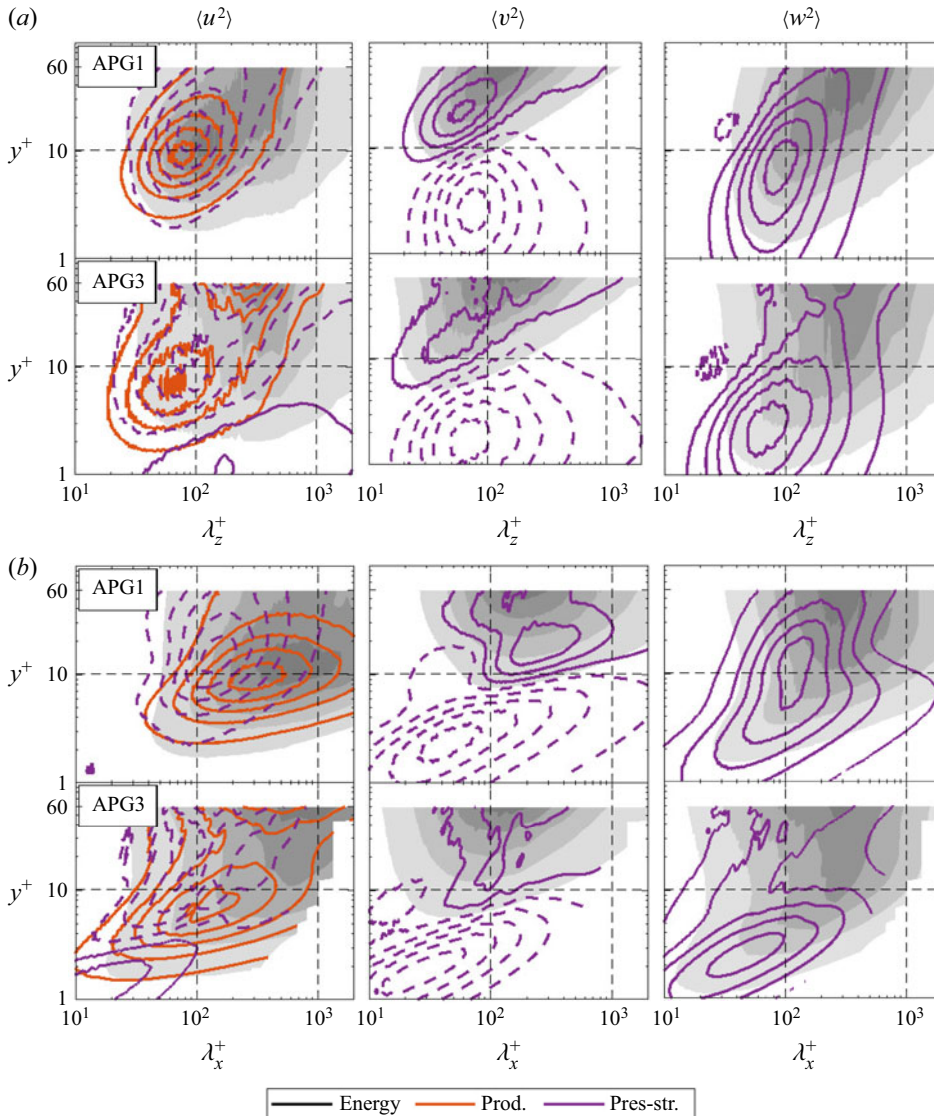


Figure 10. The premultiplied energy (shaded), production (red) and pressure-strain (purple) spectra as functions of (a) λ_z^+ and (b) λ_x^+ , and y^+ for $\langle u^2 \rangle$ (first column), $\langle v^2 \rangle$ (second column) and $\langle w^2 \rangle$ (third column). In each panel, the rows are for APG1 (top) and APG3 (bottom), respectively. The contour levels are [0.1 0.3 0.5 0.7 0.9] of the maxima of spectra in the inner layer. The dashed contours indicate negative values. The dashed lines denote $y^+ = 10$ and $\lambda^+ = 100, 1000$.

As discussed above, the velocity defect does not change significantly the spectral characteristics of the inner layer’s production and pressure-strain structures. This suggests that the well-known near-wall cycle of the canonical flows, or a turbulent regeneration mechanism with similar features to the near-wall cycle, exists in APG TBLs with small and large velocity defect. Despite the similarity of production and pressure-strain structures, the signature of inner layer streaks, which is a crucial part of the near-wall cycle, does not exist in the $\langle u^2 \rangle$ spectra of the large-defect case, as shown in figures 10 and 11. The lack of

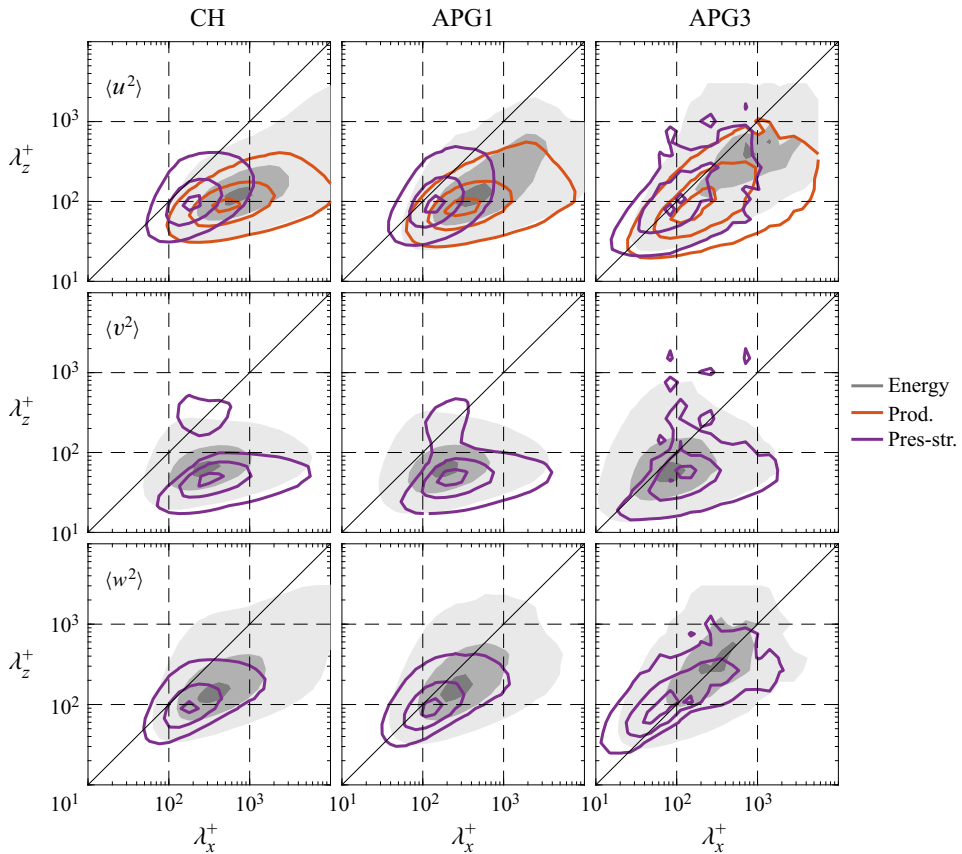


Figure 11. The premultiplied 2-D energy (shaded), production (red) and pressure-strain (purple) spectra at $y^+ \approx 13$. The columns are the channel flow, APG1 and APG3. The rows are $\langle u^2 \rangle$, $\langle v^2 \rangle$, and $\langle w^2 \rangle$. The contour levels are [0.1 0.5 0.9] of the maxima of spectra. The straight and dashed lines indicate $\lambda_x = \lambda_z$ and $\lambda_x^+ = 100$, 1000 and $\lambda_z^+ = 100$, 1000 , respectively.

this signature might be explained by large-scale outer-layer structures dominating the inner layer, as mentioned above. It is possible that the footprints of these outer-layer structures hide the signature of the inner-layer streaks in the energy spectra. A remarkable outcome emerging from this hypothesis is that the inner-layer streaks might be able to play their part in the near-wall cycle although the inner layer is dominated by much bigger structures.

5.2. Outer layer

We present now a similar analysis for the outer layer. Figure 12 displays the energy, production and pressure-strain spectra of all normal components of the Reynolds stress tensor for the small- and large-defect cases using a linear scale for y to emphasize the outer region. Moreover, the inner layer ($y/\delta < 0.1$) is masked to focus on the outer layer. Some spectral characteristics of the outer layer production and pressure-strain structures remain similar with increasing velocity defect even though the shapes of the spectra are different. For the $\langle u^2 \rangle$ component, the production and pressure-strain structures are at similar y -locations as the most energetic structures. Whereas production structures have a similar size as the most energetic structures, pressure-strain structures are slightly narrower

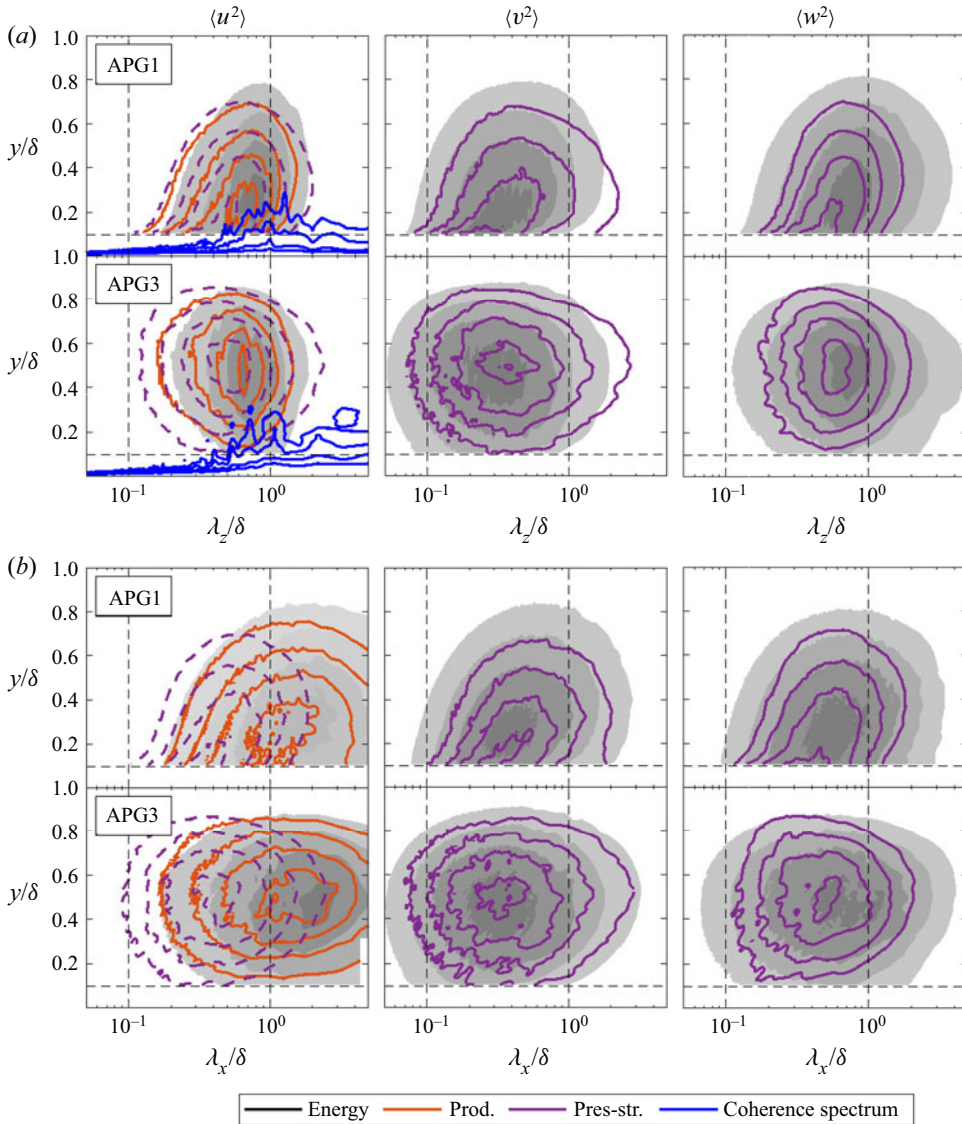


Figure 12. The premultiplied energy (shaded), production (red) and pressure-strain (purple) spectra as functions of (a) λ_z/δ and (b) λ_x/δ and y/δ for $\langle u^2 \rangle$ (first column), $\langle v^2 \rangle$ (second column) and $\langle w^2 \rangle$ (third column). In each panel, the rows are for APG1 (top) and APG3 (bottom), respectively. The contour levels are [0.1 0.3 0.5 0.7 0.9] of the maxima of spectra in the outer layer. The dashed contours indicate negative values. The dashed lines denote $y/\delta = 0.1$ and $\lambda/\delta = 0.1, 1$. The blue lines represent the coherence spectrum with contour levels [0.05 0.1 0.2 0.3].

and considerably shorter than them in both APG TBL cases. Regarding the other Reynolds stress components, the pressure-strain structures have a similar size as the most energetic structures for $\langle v^2 \rangle$, and are slightly shorter and narrower for $\langle w^2 \rangle$ than the most energetic ones. Again, these relative sizes between energetic and pressure-strain structures remain similar in both defect cases.

To examine the wall-attachment of energetic outer-layer structures, we analyse the linear coherence spectrum, which gives the coherence level between two positions in the

boundary layer for a given wavelength (Baars, Hutchins & Marusic 2017; Baars & Marusic 2020). Wall-attached structures are defined as structures whose minimum wall-normal position is in the vicinity of the wall. The coherence spectrum is computed as

$$\gamma^2(y, y_r, \lambda_z) = \frac{|\langle \hat{u}(y; \lambda_z) \hat{u}^*(y_r; \lambda_z) \rangle|^2}{\langle |\hat{u}(y; \lambda_z)|^2 \rangle \langle |\hat{u}(y_r; \lambda_z)|^2 \rangle}, \quad (5.1)$$

where $\hat{u}(y, \lambda_z)$ is the Fourier transform of the u signal at the wall-normal position y with respect to k_z , and y_r is the reference location where the coherency is considered, which is $y^+ = 2$ in the current case. The asterisk indicates the complex conjugate, and $|\cdot|$ denotes the modulus. Figure 12(a) presents the coherence spectrum for $\langle u^2 \rangle$. The coherence spectrum shows that the energetic structures in the lower part of the outer layer of APG1 are correlated to some extent with the near-wall region, albeit the correlation levels are low. The results for APG1 are very similar to the results of Tanarro *et al.* (2020) where coherence is also examined for two small-defect cases using the same reference y^+ , although the Reynolds numbers and shape factors between their cases and APG1 are slightly different from each other. In contrast, coherence between the outer peak region of the energy spectrum and the near-wall region is almost zero in APG3. These findings regarding the coherence spectrum indicate that the outer-layer energetic structures are less wall-attached in APG3 than in APG1.

In connection with wall attachment, self-similarity is another important aspect of outer-layer structures. Townsend (1976) hypothesized that the logarithmic region is populated with self-similar wall-attached eddies in wall-bounded flows, where self-similar structures are defined as structures with constant energy density and size that is proportional to their wall-normal distance. A distinctive feature of self-similar structures is the y -scaling of 1-D Reynolds shear stress cospectra, which shows that the structures' size becomes invariant when it is scaled with y (Baidya *et al.* 2017; Deshpande, Monty & Marusic 2021). The $\langle u^2 \rangle$ and $\langle v^2 \rangle$ spectra do not exhibit pure y -scaling because non-self-similar attached/detached structures contaminate the spectra. We compare the 1-D cospectra of $\langle uv \rangle$ of the APG TBL cases and the channel flow case of Lee & Moser (2015) at $Re_\tau = \delta^+ = 543$ (not the one referred to as CH throughout the paper) in figure 13. We choose a channel flow case with a Reynolds number similar to that of APG1 instead of the high-Reynolds-number case that we use throughout the paper to eliminate the effect of the Reynolds number (this is discussed further in Appendix C). Figure 13 shows the cospectra with wall-scaling and δ -scaling for APG1, APG3 and the channel flow database at several wall-normal positions. For the channel flow and APG1, the range of the wall-normal locations corresponds to the whole span of the logarithmic layer in the case of the ZPG TBL. The lower limit is $y^+ = 2.6\sqrt{\delta^+}$ (Klewicki, Fife & Wei 2009), and the upper limit is $0.2\delta^+$. In the case of APG3, we use the same wall-normal locations as APG1 because the layer structure of the boundary layer is not known for the large-defect case, and the inner layer would not scale with friction-viscous scales.

Figure 13(a) shows that the spanwise cospectra of the channel flow and APG1 scale well with y in the logarithmic region. Regarding the streamwise cospectra, δ -scaling is better than y -scaling for these two cases. This can be attributed to the low Reynolds number of these flows, as demonstrated in Appendix C. Figure 19 clearly shows that at higher Reynolds numbers, the streamwise cospectra of the channel flow scale with y and not with δ . The fact that the spanwise cospectra scale with y in APG1 suggests that self-similar structures are present in APG1 as in canonical flows.

In the case of APG3, in contrast to what happens in the channel flow case and APG1, y does not scale the spanwise cospectra. Moreover, both the spanwise and

Production and inter-component redistribution of turbulence in APG TBL

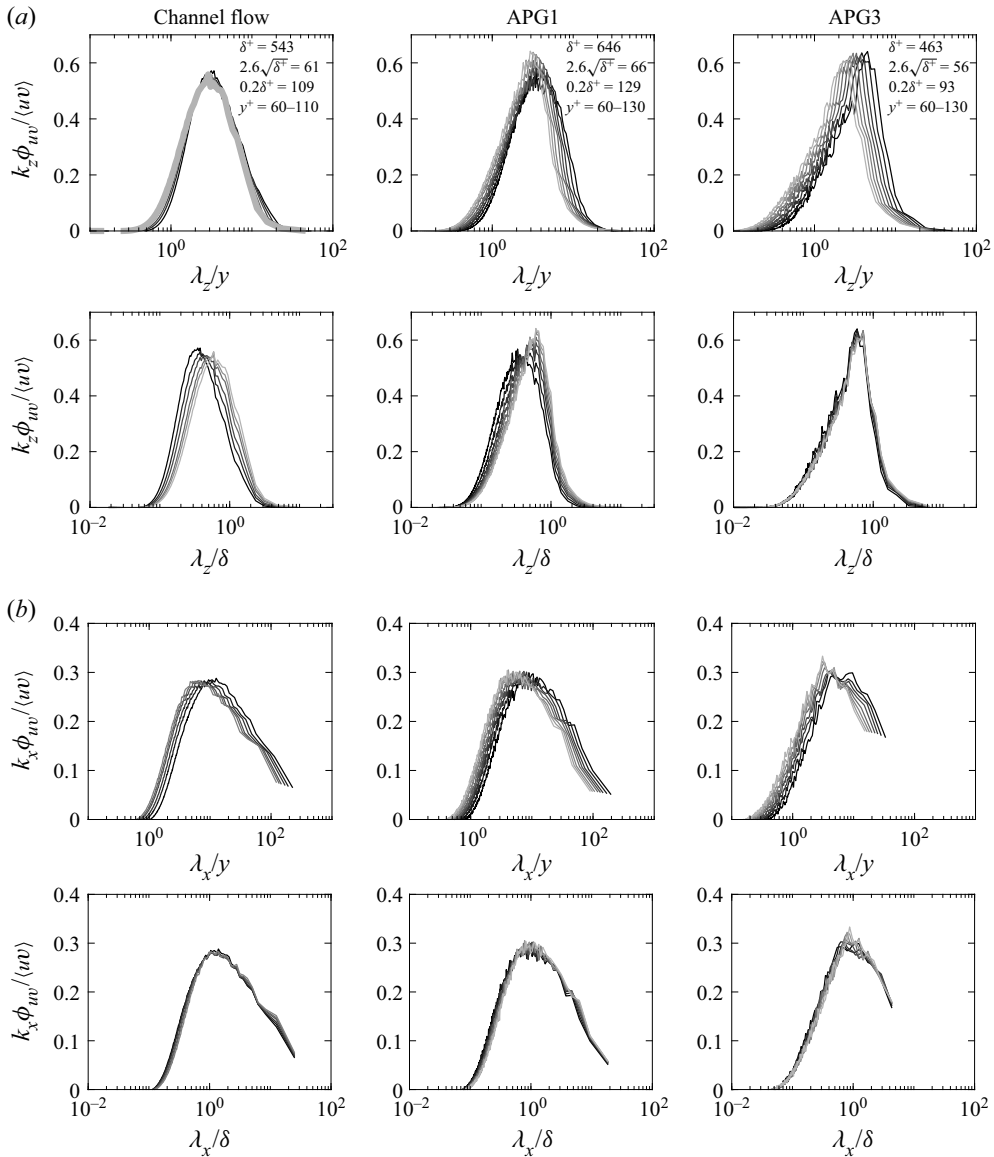


Figure 13. The premultiplied 1-D cospectra of $\langle uv \rangle$ for the channel flow case of Lee & Moser (2015) at $Re_\tau = 543$ (left), APG1 (middle) and APG3 (right) as a function of (a) λ_z , (b) λ_x , at several y -positions. The wavelength is normalized with the wall-normal distance (top row in each panel) and δ (bottom row in each panel). The spectra are normalized with local $\langle uv \rangle$. The colour becomes lighter as y increases.

streamwise cospectra of APG3 scale perfectly with δ . In addition, the 2-D spectra of APG3 (figures 6–8) demonstrate that wall distance does not scale the structures found in the lower part of the outer layer. The streamwise and spanwise wavelengths of the outer layer energetic, production and pressure-strain structures are almost the same regardless of the wall distance in the outer layer. These observations indicate that the structures do not show any self-similar characteristics, in Townsend’s sense, in the large-defect APG TBL case as far as 1-D and 2-D spectral distributions are concerned.

Another indicator of self-similarity is the relationship between λ_x and λ_z . Self-similar structures should have a linear relationship $\lambda_x \sim \lambda_z$ since this would imply that the ratio of their streamwise length to spanwise length is constant regardless of their distance to the wall. For this, we examine the 2-D spectra given in [figure 6](#), but it is important to state that only the first two y -positions shown in the figure are in the logarithmic region where we expect to see self-similar behaviour. From the energy spectra of [figure 6](#), it is found that only the highest energy contours of the $\langle v^2 \rangle$ and $\langle w^2 \rangle$ spectra follow a linear relationship of the form $\lambda_x/\lambda_z \approx 1$. Similar results were reported in the literature for channel flows (Jiménez & Hoyas 2008). In contrast, $\langle u^2 \rangle$ and $\langle uv \rangle$ spectra do not exhibit a linear $\lambda_z \sim \lambda_x$ relationship. The outer contours of the 2-D spectra for $\langle u^2 \rangle$ and $\langle uv \rangle$ follow $\lambda_z \sim \lambda_x^{1/2}$ in all cases, which is a failure of self-similarity. The square-root relationship for the outer contours of the 2-D spectra of $\langle u^2 \rangle$ was reported several times for canonical flows or small-defect APG TBLs (Del Alamo *et al.* 2004; Chandran *et al.* 2017; Tanarro *et al.* 2020). Chandran *et al.* (2017) demonstrated that this behaviour occurs when the Reynolds number is low. They found that the $\langle u^2 \rangle$ spectra of the ZPG TBL exhibit the linear relationship $\lambda_z \sim \lambda_x$ at sufficiently high Reynolds number.

The findings about coherency and scaling of the spectra suggest that the outer layer of the large-defect case is populated with detached structures not affected by the wall. The presence of wall-detached structures in APG TBLs was suggested by Perry & Marusic (1995) in their attached-eddy model. Moreover, it was demonstrated that the wall-attached structures are weaker and less numerous in large-defect APG TBLs than in ZPG TBLs (Maciel *et al.* 2017a), and the contribution of wall-detached structures to Reynolds stresses increases in APG TBLs (Maciel *et al.* 2017a; Yoon *et al.* 2020). Also, it has been reported that the wall-detached structures in the outer layer are much more independent of the wall in channel flows or APG TBLs than the wall-attached ones, and are similar to structures in homogeneous shear turbulence (Dong *et al.* 2017; Gungor *et al.* 2020). Therefore, it can be concluded that the outer layer of the large-defect case is dominated by structures that are not affected significantly by the wall, which is not the case in the small-defect case. The dominance of wall-detached structures also suggests that the outer layers of APG TBLs could behave like free shear flows (Gungor *et al.* 2016).

Despite the differences between the outer layers of the small- and large-defect cases discussed above, many spectral characteristics of production and pressure-strain structures remain similar regardless of the velocity defect. [Figures 14–16](#) show the 2-D spectra of energy, production and pressure-strain for the channel flow, APG1 and APG3 at $y/\delta = 0.15$ and 0.50 . These two wall-normal positions are the positions with significant energy and energy transfer in the case of APG1 ($y/\delta = 0.15$) and APG3 ($y/\delta = 0.50$). The 2-D spectra of energy, production and pressure-strain have strikingly similar characteristics in all flow cases at both wall-normal positions. Their shapes, wavelength aspect ratios and relative sizes do not change significantly with velocity defect. Whereas the size of structures remains almost unchanged at $y/\delta = 0.15$ in all flow cases, all structures decrease in size with increasing velocity defect at $y/\delta = 0.50$. This decrease of size in the outer flow might be due to the decreasing presence of wall-attached structures. Indeed, at that height, wall-attached structures are big since they scale with y .

Even though the dominant dynamic role in the outer layer may shift from wall-attached to wall-detached structures as the defect increases, the striking spectral similarities between all flows shown in [figures 14–16](#) suggest that the production and inter-component energy transfer mechanisms might still be the same. This is consistent with the observation by Dong *et al.* (2017) that the fact that dynamically relevant structures are attached to the wall in channel flows is not the reason for their dynamic relevance. Wall attachment could

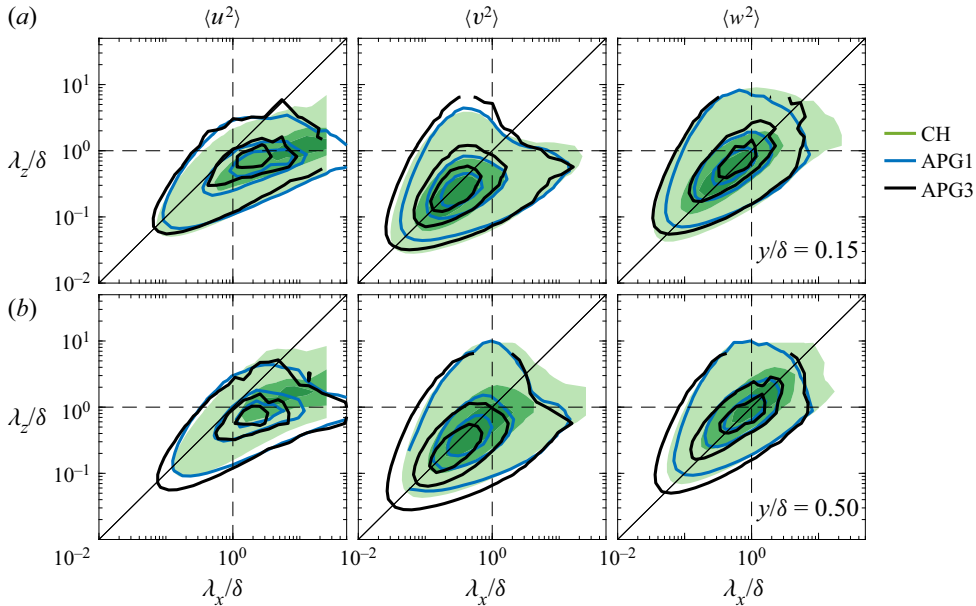


Figure 14. The premultiplied 2-D energy spectra of CH (green), APG1 (blue) and APG3 (black) at (a) $y/\delta = 0.15$ and (b) $y/\delta = 0.5$. The columns are $\langle u^2 \rangle$, $\langle v^2 \rangle$ and $\langle w^2 \rangle$. The contour levels are [0.1 0.5 0.8] of the maxima of spectra.

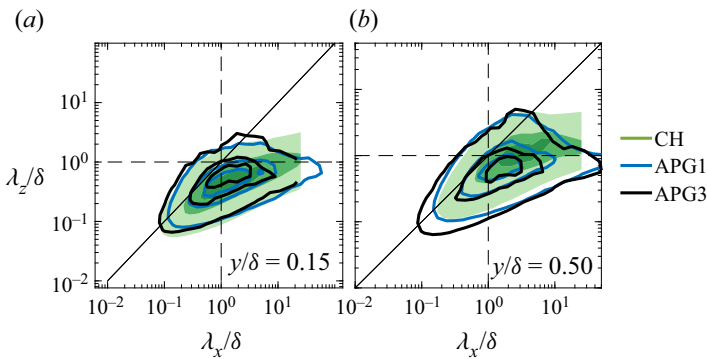


Figure 15. The premultiplied 2-D production spectra of $\langle u^2 \rangle$ at (a) $y/\delta = 0.15$ and (b) $y/\delta = 0.5$, for CH (green), APG1 (blue) and APG3 (black). The contour levels are [0.1 0.5 0.8] of the maxima of spectra.

only be a consequence of their size. Therefore, in the outer region of wall-bounded flows, the energy transfer mechanisms might remain the same no matter if dynamically relevant structures are attached to or detached from the wall.

The reason for the increase of relative importance of the outer layer with respect to the inner layer might be the change in the mean shear since the spectral analysis suggests that the production mechanisms remain similar in all the considered flows. As shown previously with figures 2(c) and 2(d), with increasing velocity defect, mean shear increases significantly in the outer layer (normalized with the outer scales), while it remains fairly constant in the inner layer (normalized with the inner scales) in comparison. Consistently with this trend, the outer-layer turbulence becomes dominant as the mean shear in the outer

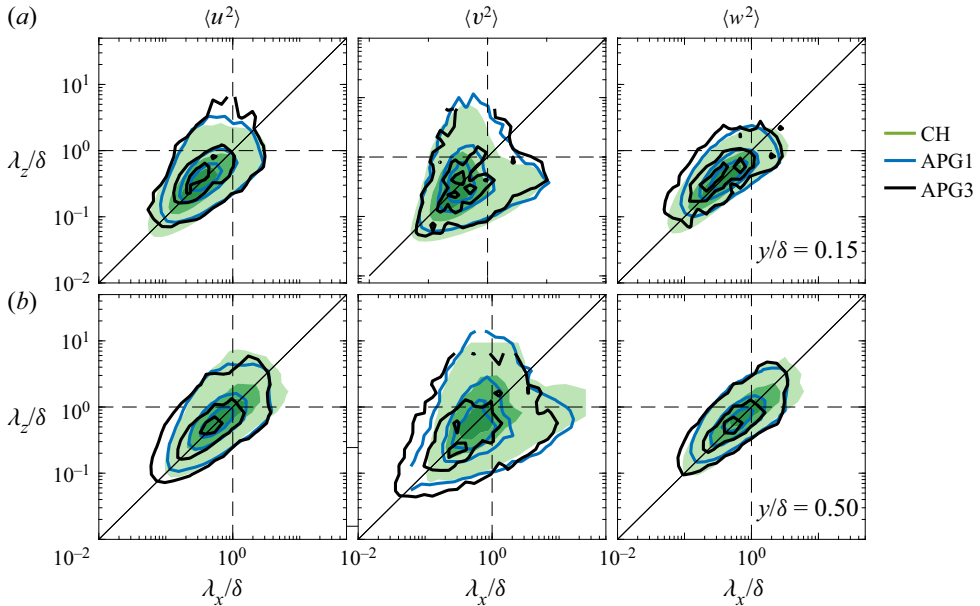


Figure 16. The premultiplied 2-D pressure-strain spectra of CH (green), APG1 (blue) and APG3 (black) at (a) $y/\delta = 0.15$ and (b) $y/\delta = 0.5$. The columns are $\langle u^2 \rangle$, $\langle v^2 \rangle$ and $\langle w^2 \rangle$. The contour levels are [0.1 0.5 0.8] of the maxima of spectra.

layer increases. This trend becomes more apparent as the defect becomes large. Moreover, the present analysis shows that none of the cases examined here exhibits a peak in the $\langle v^2 \rangle$ spectra with a frequency corresponding to a certain Strouhal number that would signal the presence of inflection type instabilities, although the existence of such types of instabilities in APG TBLs was reported (Elsberry *et al.* 2000). This suggests that these instability mechanisms do not affect the flow importantly or exist at all. The magnitude of the mean shear appears to be the main reason for the increase in relative importance of the outer layer activity in APG TBLs.

6. Conclusions

In the current study, we have examined production and redistribution energy transfer mechanisms and coherent structures that are active in these mechanisms or carry energy in APG TBLs, and compared them with those of channel flows and ZPG TBLs. For this purpose, we have utilized the spectral distributions of energy, production and pressure-strain of the Reynolds stress tensor components.

The results show that spectral features of Reynolds stresses, production and pressure-strain are similar in the inner layer of APG TBLs and canonical wall-bounded flows. The inner-scaled wall-normal location of the well-known inner peak of $\langle u^2 \rangle$ is the same in the small-defect APG TBL case and canonical wall-bounded flows. Moreover, energetic and production structures in the inner layer have comparable spanwise wavelengths, although the streamwise length of structures is shorter in the APG TBL case than in canonical flows. When the outer layer is masked, the shapes of the production and pressure-strain spectra in the inner layer are very similar in the small- and large-defect cases, although there is no inner peak for the energy spectra of $\langle u^2 \rangle$ in the large-defect case.

In addition, the 2-D spectra of production and pressure-strain in the inner layer show similar streamwise–spanwise characteristics in the channel flow and both APG TBL cases.

The near-wall cycle, or another turbulence regeneration mechanism that works in a similar way to the near-wall cycle, appears to exist in the large-defect case. Interestingly, it would be present while the characteristic streaks are not the dominant structures considering their signature is absent in the energy spectra. This can be possible in two ways. The first is that this regeneration mechanism does not need the streaks, which is rather unlikely considering the overall similarities between the flow cases. The other is that the big outer-layer structures dominate the inner layer in the large-defect case in a way that the spectra do not exhibit the streak-related inner peak, but the streaks would nonetheless be present. Interestingly, this would mean that the streaks continue playing their role in turbulence regeneration even if they are amid bigger and more energetic structures.

In the outer region, the wall-normal distributions of energy, production and pressure-strain spectra are different between canonical flows and APG TBLs with small and large velocity defects. The reason for this difference is that the relative intensity of the inner and outer layer turbulent activity changes considerably with increasing velocity defect, from dominant inner turbulence to dominant outer turbulence. In addition, the spectra suggest that wall-detached structures may play a more important dynamic role in large-defect APG TBLs than in small-defect APG TBLs or canonical flows. Due to this, the outer layer of large-defect APG TBLs is less affected by the wall than in small-defect flows. As a result, it appears to act more like a free shear layer than a wall-bounded flow. Despite these differences, the production and inter-component energy transfer mechanisms might still be similar in all flow cases. The 2-D spectra have strikingly similar features in the outer regions of all flows, such as shape and wavelength aspect ratios, as well as relative sizes between energy, production and pressure-strain structures. This suggests that the distinction between wall-attached structures in small-defect flows and wall-detached structures in large-defect flows is not important in a dynamical sense.

Strong mean shear in the outer layer seems to be the primary reason for the elevated outer-layer activity in the APG TBL cases. The change of the wall-normal distribution of the Reynolds stresses, production and pressure-strain is consistent with the change of the mean shear with increasing velocity defect. Furthermore, that the spectral analysis does not show any significant difference between the energetic, production and pressure-strain structures in channel flows and APG TBLs suggests that inflection-type instabilities such as the Kelvin–Helmholtz instability either do not exist or are weak compared to other shear-driven mechanisms. Moreover, the $\langle v^2 \rangle$ spectra of the large-defect APG TBL do not reveal any sign of an inflection-type instability. However, further work is necessary to confirm the presence or absence of inflection-type or other types of instabilities.

The upstream history of the flow probably affects the coherent structures, but it is challenging to isolate history effects of the pressure gradient on the coherent structures from its local effects. However, the comparison of the present APG TBL with equilibrium APG TBLs found in the literature indicates that the spectral properties of structures with increasing velocity defect are similar in both equilibrium and non-equilibrium cases. Nonetheless, more work and other databases are required to understand the history effect in a more precise manner.

The overall conclusion is that the mechanisms producing turbulence and those responsible for inter-component energy transfer may remain the same within one layer as the velocity defect increases. What makes the large-defect boundary layer different from the small-defect one seems to be mainly that the mechanisms in the inner layer decay

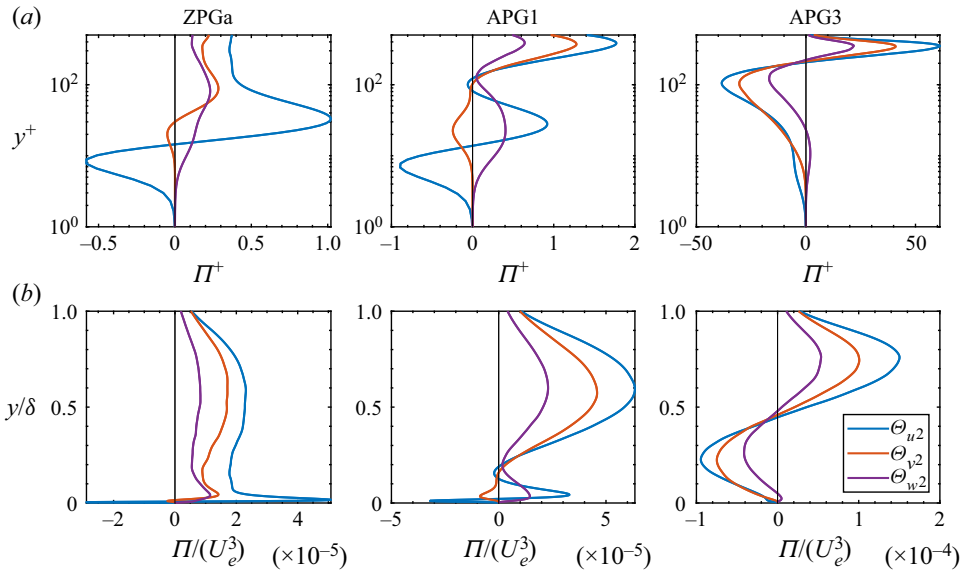


Figure 17. The Reynolds stress flux in the wall-normal direction as a function of y . The parameters are normalized with (a) the friction-viscous scales and (b) the outer scales. The columns are respectively ZPGa, APG1 and APG3.

significantly in importance with respect to the outer ones with increasing velocity defect. It remains to be confirmed if this is solely due to the changes in the mean shear in each region or if other factors are at play.

To reach a more solid conclusion regarding energy transfer in APG TBLs, inter-scale energy transfer should be investigated in a similar manner to the current study. Moreover, this study provides a perspective from a statistical and spectral point of view, and further studies examining dynamic properties of coherent structures in APG TBLs, preferably at higher Reynolds numbers, would help us to understand energy transfer mechanisms in APG TBLs in more detail.

Acknowledgements. We acknowledge PRACE for awarding us access to Marconi100 at CINECA, Italy, and Calcul Québec (www.calculquebec.ca) and Compute Canada (www.computeCanada.ca) for awarding us access to the Niagara HPC server. The authors would like to thank Myoungkyu Lee and Robert D. Moser for providing their channel flow data.

Funding. T.R.G. and A.G.G. were supported by the research funds of Istanbul Technical University (project nos MGA-2019-42227 and MDK-2018-41689). T.R.G. and Y.M. acknowledge the support of the Natural Sciences and Engineering Research Council of Canada (NSERC), project no. RGPIN-2019-04194.

Declaration of interests. The authors report no conflict of interest.

Author ORCIDs.

Taygun R. Gungor <https://orcid.org/0000-0002-3143-8254>;

Yvan Maciel <https://orcid.org/0000-0003-1993-472X>;

Ayse G. Gungor <https://orcid.org/0000-0002-3501-9516>.

Appendix A. The Reynolds stress flux

Figure 17 shows the the Reynolds stress fluxes due to turbulent transport in the wall-normal direction $\theta_{ii} = \langle u_i u_i u_2 \rangle$ for ZPGa, APG1 and APG3. They are discussed in § 3.3.

Production and inter-component redistribution of turbulence in APG TBL

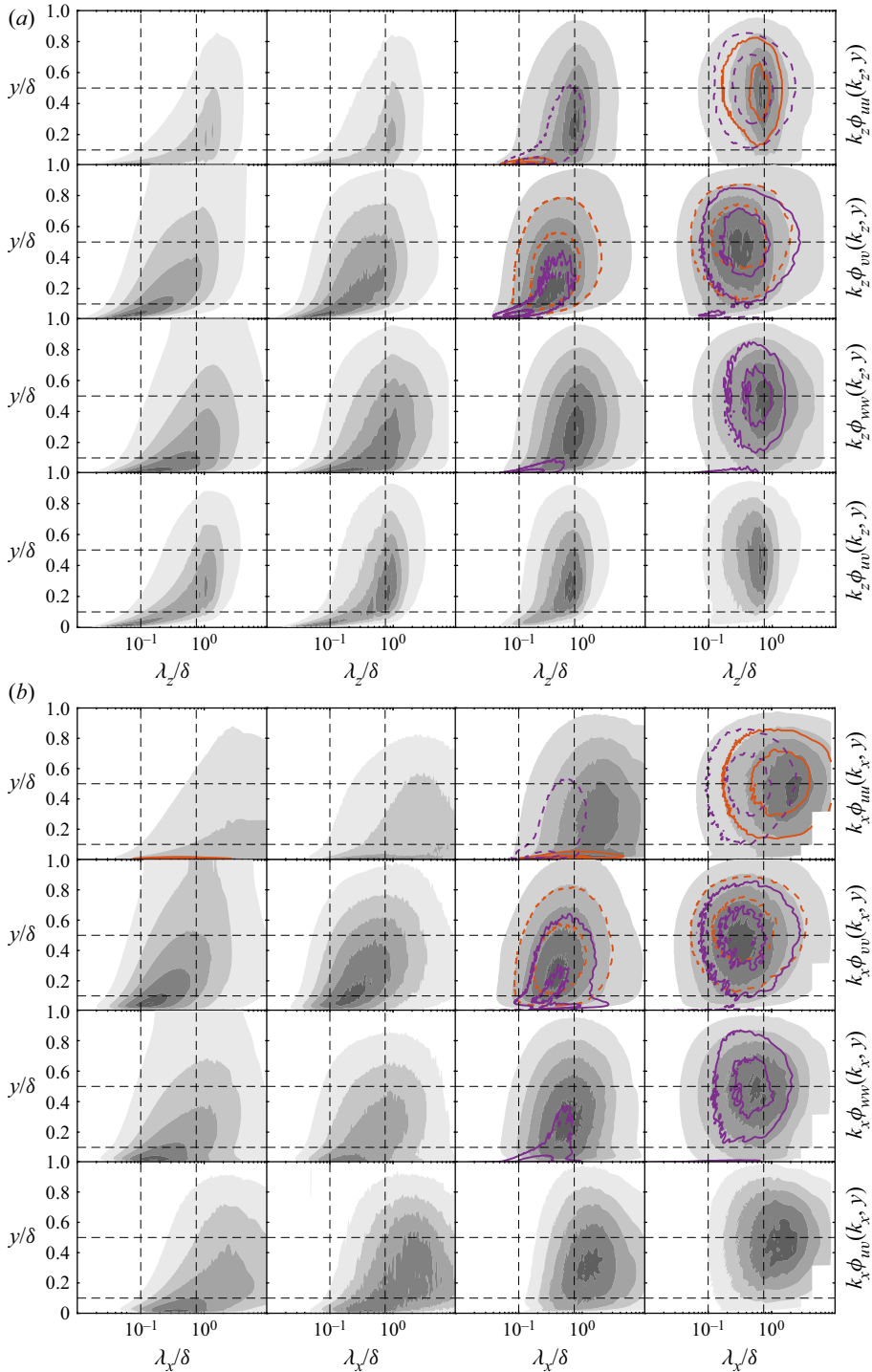


Figure 18. The premultiplied 1-D energy (shaded contours), production (red contours) and pressure-strain (purple contours) spectra of the channel flow (first column), the ZPG TBLs (second column), APG1 (third column) and APG3 (fourth column) as functions of (a) λ_z/δ and (b) λ_x/δ , and y/δ . The rows of each panel are respectively $\langle u^2 \rangle$, $\langle v^2 \rangle$, $\langle w^2 \rangle$ and $\langle uv \rangle$. The contour levels are [0.1 0.3 0.5 0.7 0.9] of the maxima of spectra for energy, and [0.3 0.7] of the maxima of spectra for production and pressure-strain. The dashed contours indicate negative values. The horizontal and vertical dashed lines indicate $y/\delta = 0.1, 0.5$ and $\lambda/\delta = 0.1, 0.75$.

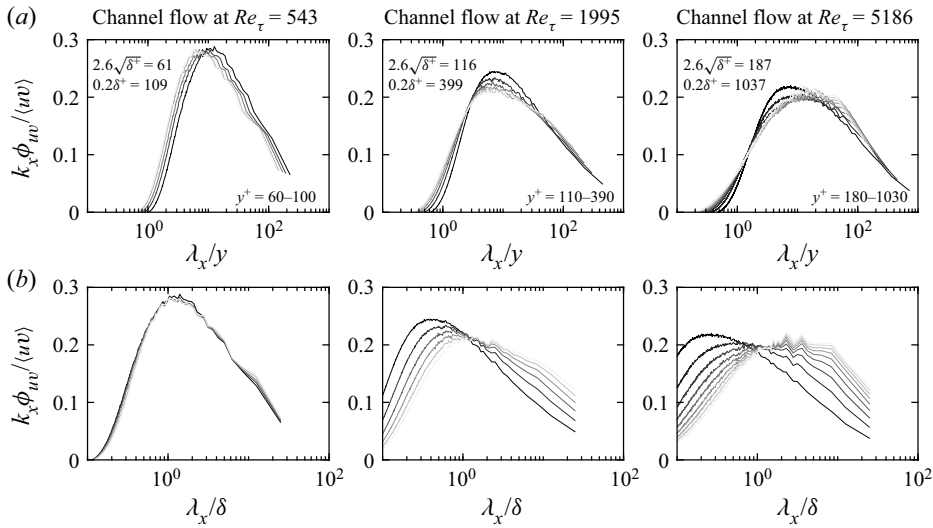


Figure 19. The cospectra for three channel flow cases of Lee & Moser (2015). The streamwise wavelength is normalized with (a) y and (b) δ , and the spectra are normalized with local $\langle uv \rangle$. The spectra are plotted in the log region and the limits are $y^+ = 2.6\sqrt{\delta^+}$ and $0.2\delta^+$. The colour becomes lighter as y increases.

Appendix B. The premultiplied outer-scaled spectra

Figure 18 shows the spectral distributions of energy, production and pressure-strain as functions of y/δ and wavelength components λ_x/δ and λ_z/δ for all components of the Reynolds stress tensor. The y -axis is linear to show the outer layer in more detail. Each spectral distribution is normalized with its respective maximum.

Appendix C. Effect of Re on the scaling of the streamwise cospectra

Figure 19 presents the cospectra for three channel flow cases of Lee & Moser (2015) at different Re_τ to examine the effect of the Reynolds number on the scaling of the streamwise cospectra. Although δ scales well the cospectra in the low- Re case, it fails to do so in the high- Re cases. In the latter cases, the cospectra scale approximately with y for $\lambda_x > 2y$. That cospectra are scaled by y in high- Re cases was also shown by Baidya *et al.* (2017).

REFERENCES

- BAARS, W.J., HUTCHINS, N. & MARUSIC, I. 2017 Self-similarity of wall-attached turbulence in boundary layers. *J. Fluid Mech.* **823**, R2.
- BAARS, W.J. & MARUSIC, I. 2020 Data-driven decomposition of the streamwise turbulence kinetic energy in boundary layers. Part 1. Energy spectra. *J. Fluid Mech.* **882**, A25.
- BAIDYA, R., PHILIP, J., HUTCHINS, N., MONTY, J.P. & MARUSIC, I. 2017 Distance-from-the-wall scaling of turbulent motions in wall-bounded flows. *Phys. Fluids* **29** (2), 020712.
- BAIDYA, R., PHILIP, J., HUTCHINS, N., MONTY, J.P. & MARUSIC, I. 2021 Spanwise velocity statistics in high-Reynolds-number turbulent boundary layers. *J. Fluid Mech.* **913**, A35.
- BALANTRAPU, N.A., HICKLING, C., ALEXANDER, W.N. & DEVENPORT, W. 2021 The structure of a highly decelerated axisymmetric turbulent boundary layer. *J. Fluid Mech.* **929**, A9.
- BOBKE, A., VINUESA, R., ÖRLÜ, R. & SCHLATTER, P. 2017 History effects and near equilibrium in adverse-pressure-gradient turbulent boundary layers. *J. Fluid Mech.* **820**, 667–692.

- BORRELL, G., SILLERO, J.A. & JIMÉNEZ, J. 2013 A code for direct numerical simulation of turbulent boundary layers at high Reynolds numbers in BG/P supercomputers. *Comput. Fluids* **80**, 37–43.
- CHAN, C.I., SCHLATTER, P. & CHIN, R.C. 2021 Interscale transport mechanisms in turbulent boundary layers. *J. Fluid Mech.* **921**, A13.
- CHANDRAN, D., BAIDYA, R., MONTY, J.P. & MARUSIC, I. 2017 Two-dimensional energy spectra in high-Reynolds-number turbulent boundary layers. *J. Fluid Mech.* **826**, R1.
- CHO, M., HWANG, Y. & CHOI, H. 2018 Scale interactions and spectral energy transfer in turbulent channel flow. *J. Fluid Mech.* **854**, 474–504.
- DEL ALAMO, J.C., JIMÉNEZ, J., ZANDONADE, P. & MOSER, R.D. 2004 Scaling of the energy spectra of turbulent channels. *J. Fluid Mech.* **500**, 135–144.
- DESHPANDE, R., MONTY, J.P. & MARUSIC, I. 2021 Active and inactive components of the streamwise velocity in wall-bounded turbulence. *J. Fluid Mech.* **914**, A5.
- DONG, S., LOZANO-DURÁN, A., SEKIMOTO, A. & JIMÉNEZ, J. 2017 Coherent structures in statistically stationary homogeneous shear turbulence. *J. Fluid Mech.* **816**, 167–208.
- ELSBERRY, K., LOEFFLER, J., ZHOU, M.D. & WYGNANSKI, I. 2000 An experimental study of a boundary layer that is maintained on the verge of separation. *J. Fluid Mech.* **423**, 227–261.
- GATTI, D., CHIARINI, A., CIMARELLI, A. & QUADRIO, M. 2020 Structure function tensor equations in inhomogeneous turbulence. *J. Fluid Mech.* **898**, A5.
- GRIFFIN, K.P., FU, L. & MOIN, P. 2021 General method for determining the boundary layer thickness in nonequilibrium flows. *Phys. Rev. Fluids* **6** (2), 024608.
- GUNGOR, A.G., MACIEL, Y., SIMENS, M.P. & GUNGOR, T.R. 2017 Direct numerical simulation of a non-equilibrium adverse pressure gradient boundary layer up to $Re_\theta = 8000$. In *16th European Turbulence Conference, Stockholm, Sweden*. European Mechanics Society.
- GUNGOR, A.G., MACIEL, Y., SIMENS, M.P. & SORIA, J. 2016 Scaling and statistics of large-defect adverse pressure gradient turbulent boundary layers. *Intl J. Heat Fluid Flow* **59**, 109–124.
- GUNGOR, T.R., MACIEL, Y. & GUNGOR, A.G. 2020 Reynolds shear-stress carrying structures in shear-dominated flows. *J. Phys.: Conf. Ser.* **1522** (1), 012009.
- HALL, P. & HORSEMAN, N.J. 1991 The linear inviscid secondary instability of longitudinal vortex structures in boundary layers. *J. Fluid Mech.* **232**, 357–375.
- HARUN, Z., MONTY, J.P., MATHIS, R. & MARUSIC, I. 2013 Pressure gradient effects on the large-scale structure of turbulent boundary layers. *J. Fluid Mech.* **715**, 477–498.
- HUTCHINS, N. & MARUSIC, I. 2007a Evidence of very long meandering features in the logarithmic region of turbulent boundary layers. *J. Fluid Mech.* **579**, 1–28.
- HUTCHINS, N. & MARUSIC, I. 2007b Large-scale influences in near-wall turbulence. *Phil. Trans. R. Soc. A* **365** (1852), 647–664.
- JIMÉNEZ, J. & HOYAS, S. 2008 Turbulent fluctuations above the buffer layer of wall-bounded flows. *J. Fluid Mech.* **611**, 215–236.
- KAWATA, T. & ALFREDSSON, P.H. 2018 Inverse interscale transport of the Reynolds shear stress in plane Couette turbulence. *Phys. Rev. Lett.* **120**, 244501.
- KIM, K.C. & ADRIAN, R.J. 1999 Very large-scale motion in the outer layer. *Phys. Fluids* **11** (2), 417–422.
- KITSIOS, V., ATKINSON, C., SILLERO, J.A., BORRELL, G., GUNGOR, A.G., JIMÉNEZ, J. & SORIA, J. 2016 Direct numerical simulation of a self-similar adverse pressure gradient turbulent boundary layer. *Intl J. Heat Fluid Flow* **61**, 129–136.
- KITSIOS, V., SEKIMOTO, A., ATKINSON, C., SILLERO, J.A., BORRELL, G., GUNGOR, A.G., JIMÉNEZ, J. & SORIA, J. 2017 Direct numerical simulation of a self-similar adverse pressure gradient turbulent boundary layer at the verge of separation. *J. Fluid Mech.* **829**, 392–419.
- KLEWICKI, J., FIFE, P. & WEI, T. 2009 On the logarithmic mean profile. *J. Fluid Mech.* **638**, 73–93.
- LEE, J.H. 2017 Large-scale motions in turbulent boundary layers subjected to adverse pressure gradients. *J. Fluid Mech.* **810**, 323–361.
- LEE, J.H. & SUNG, H.J. 2009 Structures in turbulent boundary layers subjected to adverse pressure gradients. *J. Fluid Mech.* **639**, 101–131.
- LEE, M. & MOSER, R.D. 2015 Direct numerical simulation of turbulent channel flow up to $Re_\tau \approx 5200$. *J. Fluid Mech.* **774**, 395–415.
- LEE, M. & MOSER, R.D. 2019 Spectral analysis of the budget equation in turbulent channel flows at high Reynolds number. *J. Fluid Mech.* **860**, 886–938.
- LUMLEY, J.L. 1964 Spectral energy budget in wall turbulence. *Phys. Fluids* **7** (2), 190–196.
- MACIEL, Y., GUNGOR, A.G. & SIMENS, M. 2017a Structural differences between small and large momentum-defect turbulent boundary layers. *Intl J. Heat Fluid Flow* **67**, 95–110.

- MACIEL, Y., ROSSIGNOL, K.S. & LEMAY, J. 2006a Self-similarity in the outer region of adverse-pressure-gradient turbulent boundary layers. *AIAA J.* **44** (11), 2450–2464.
- MACIEL, Y., ROSSIGNOL, K.S. & LEMAY, J. 2006b A study of a turbulent boundary layer in stalled-airfoil-type flow conditions. *Exp. Fluids* **41** (4), 573–590.
- MACIEL, Y., SIMENS, M.P. & GUNGOR, A.G. 2017b Coherent structures in a non-equilibrium large-velocity-defect turbulent boundary layer. *Flow Turbul. Combust.* **98** (1), 1–20.
- MACIEL, Y., WEI, T., GUNGOR, A.G. & SIMENS, M.P. 2018 Outer scales and parameters of adverse-pressure-gradient turbulent boundary layers. *J. Fluid Mech.* **844**, 5–35.
- MANSOUR, N.N., KIM, J. & MOIN, P. 1988 Reynolds-stress and dissipation-rate budgets in a turbulent channel flow. *J. Fluid Mech.* **194**, 15–44.
- MARQUILLIE, M., EHRENSTEIN, U. & LAVAL, J.P. 2011 Instability of streaks in wall turbulence with adverse pressure gradient. *J. Fluid Mech.* **681**, 205–240.
- MARUSIC, I., MATHIS, R. & HUTCHINS, N. 2010a High Reynolds number effects in wall turbulence. *Intl J. Heat Fluid Flow* **31** (3), 418–428.
- MARUSIC, I., MCKEON, B.J., MONKEWITZ, P.A., NAGIB, H.M., SMITS, A.J. & SREENIVASAN, K.R. 2010b Wall-bounded turbulent flows at high Reynolds numbers: recent advances and key issues. *Phys. Fluids* **22** (6), 065103.
- MATHIS, R., MONTY, J.P., HUTCHINS, N. & MARUSIC, I. 2009 Comparison of large-scale amplitude modulation in turbulent boundary layers, pipes, and channel flows. *Phys. Fluids* **21** (11), 111703.
- MIZUNO, Y. 2016 Spectra of energy transport in turbulent channel flows for moderate Reynolds numbers. *J. Fluid Mech.* **805**, 171–187.
- PERRY, A.E. & MARUSIC, I. 1995 A wall-wake model for the turbulence structure of boundary layers. Part 1. Extension of the attached eddy hypothesis. *J. Fluid Mech.* **298**, 361–388.
- RAHGOZAR, S. & MACIEL, Y. 2012 Statistical analysis of low- and high-speed large-scale structures in the outer region of an adverse pressure gradient turbulent boundary layer. *J. Turbul.* **13**, N46.
- SANMIGUEL VILA, C., VINUESA, R., DISCETTI, S., IANIRO, A., SCHLATTER, P. & ÖRLÜ, R. 2020a Separating adverse-pressure-gradient and Reynolds-number effects in turbulent boundary layers. *Phys. Rev. Fluids* **5**, 064609.
- SANMIGUEL VILA, C., VINUESA, R., DISCETTI, S., IANIRO, A., SCHLATTER, P. & ÖRLÜ, R. 2020b Experimental realisation of near-equilibrium adverse-pressure-gradient turbulent boundary layers. *Exp. Therm. Fluid Sci.* **112**, 109975.
- SCHATZMAN, D.M. & THOMAS, F.O. 2017 An experimental investigation of an unsteady adverse pressure gradient turbulent boundary layer: embedded shear layer scaling. *J. Fluid Mech.* **815**, 592–642.
- SILLERO, J.A., JIMÉNEZ, J. & MOSER, R.D. 2013 One-point statistics for turbulent wall-bounded flows at Reynolds numbers up to $\delta^+ \approx 2000$. *Phys. Fluids* **25** (10), 105102.
- SIMENS, M.P., JIMÉNEZ, J., HOYAS, S. & MIZUNO, Y. 2009 A high-resolution code for turbulent boundary layers. *J. Comput. Phys.* **228** (11), 4218–4231.
- SKÅRE, P.E. & KROGSTAD, P. 1994 A turbulent equilibrium boundary layer near separation. *J. Fluid Mech.* **272**, 319–348.
- SKOTE, M. & HENNINGSON, D.S. 2002 Direct numerical simulation of a separated turbulent boundary layer. *J. Fluid Mech.* **471**, 107–136.
- SMITS, A.J., MCKEON, B.J. & MARUSIC, I. 2011 High-Reynolds number wall turbulence. *Annu. Rev. Fluid Mech.* **43**, 353–375.
- TANARRO, Á., VINUESA, R. & SCHLATTER, P. 2020 Effect of adverse pressure gradients on turbulent wing boundary layers. *J. Fluid Mech.* **883**, A8.
- TOWNSEND, A.A. 1976 *The Structure of Turbulent Shear Flow*. Cambridge University Press.
- YOON, M., HWANG, J., YANG, J. & SUNG, H.J. 2020 Wall-attached structures of streamwise velocity fluctuations in an adverse-pressure-gradient turbulent boundary layer. *J. Fluid Mech.* **885**, A12.
- ZAGAROLA, M.V. & SMITS, A.J. 1998 Mean-flow scaling of turbulent pipe flow. *J. Fluid Mech.* **373**, 33–79.